UCSF

UC San Francisco Previously Published Works

Title

Clock-Generated Temporal Codes Determine Synaptic Plasticity to Control Sleep.

Permalink

https://escholarship.org/uc/item/91x9p66m

Journal

Cell, 175(5)

Authors

Tabuchi, Masashi
Monaco, Joseph
Duan, Grace
et al.

Publication Date

2018-11-15

DOI

10.1016/j.cell.2018.09.016

Peer reviewed

Clock-Generated Temporal Codes Determine Synaptic Plasticity to Control Sleep

Masashi Tabuchi[1], **Joseph D. Monaco**[2], **Grace Duan**[1], **Benjamin Bell**[3], **Sha Liu**[4], **Qili Liu**[1], **Kechen Zhang**[2,5], and **Mark N. Wu**[1,5,6,*]

[1]Department of Neurology, Johns Hopkins University, Baltimore, MD 21205

[2]Department of Biomedical Engineering, Johns Hopkins University, Baltimore, MD 21205

[3]McKusick-Nathans Institute of Genetic Medicine, Johns Hopkins University, Baltimore, MD 21205

[4]VIB Center for Brain and Disease Research and Department of Neuroscience, KU Leuven, Leuven, 3000, Belgium

[5]Solomon H. Snyder Department of Neuroscience, Johns Hopkins University, Baltimore, MD 21205

[6]Lead contact

Summary

Neurons use two main schemes to encode information: rate coding (frequency of firing) and temporal coding (timing or pattern of firing). While the importance of rate coding is well-established, it remains controversial whether temporal codes alone are sufficient for controlling behavior. Moreover, the molecular mechanisms underlying the generation of specific temporal codes are enigmatic. Here, we show in *Drosophila* clock neurons that distinct temporal spike patterns, dissociated from changes in firing rate, encode time-dependent arousal and regulate sleep. From a large-scale genetic screen, we identify the molecular pathways mediating the circadian-dependent changes in ionic flux and spike morphology that rhythmically modulate spike timing. Remarkably, the daytime spiking pattern alone is sufficient to drive plasticity in downstream arousal neurons, leading to increased firing of these cells. These findings demonstrate a causal role for temporal coding in behavior and define a form of synaptic plasticity triggered solely by temporal spike patterns.

In Brief

Temporal patterns of Drosophila clock neuron firing are sufficient to drive synaptic plasticity, impacting neuronal function and behavior.

Graphical Abstract
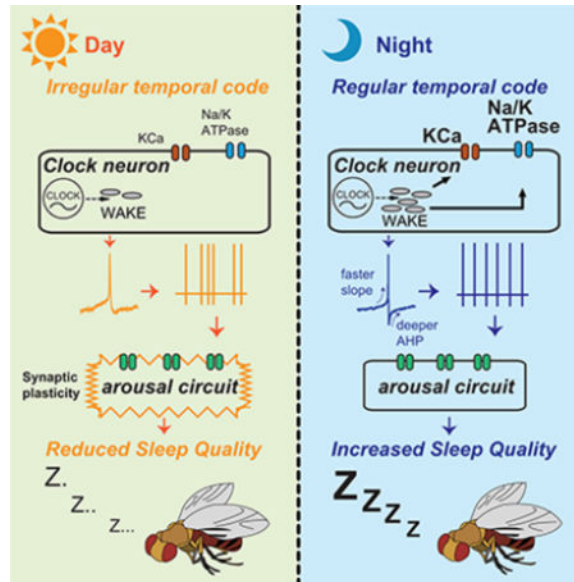
Keywords

Temporal coding; synaptic plasticity; sleep; circadian clock; *Drosophila*

Introduction

Understanding how the brain represents and processes information is a fundamental goal of neuroscience research. For the first half of the 20th century, the dominant neural coding model postulated that simple action potential (spike) counts in the relevant time window encode information about the environment or internal states (i.e., the rate coding model) (Adrian and Zotterman, 1926a, b; Stein, 1967). However, it has long been recognized that neural coding schemes using temporal codes (timing and/or pattern of spiking) would be computationally more powerful than traditional rate codes (MacKay and McCulloch, 1952). In contrast to rate coding, which comprises a singular mechanism, temporal coding encompasses a diverse repertoire of coding schemes in individual or groups of neurons, ranging from latency to first spike to synchronization of oscillatory activity between spatially segregated neuronal populations (Rieke et al., 1997).

A wide variety of temporal codes have now been observed to correlate with specific external stimuli in different settings, including sensory systems, hippocampal place cells, and neocortical circuits (Gollisch and Meister, 2008; Gray et al., 1989; Laurent and Davidowitz, 1994; Skaggs et al., 1996). However, the assessment of whether and how temporal codes embody neurobiologically relevant information is complicated by multiple factors, such as the concomitant presence of changes in firing rate, integration of spatial with temporal

information, and the requirement for multiple interacting brain regions in the regulation of behavior (Baranauskas, 2015; Panzeri et al., 2010). The rigorous demonstration of a causal role for temporal codes in representing biological information requires the fulfillment of three criteria (Chong and Rinberg, 2018; Panzeri et al., 2017). First, the temporal code should exist under native conditions or be elicited by naturalistic stimuli. Second, as articulated in the "reader-actuator" model proposed by Buzsáki (Buzsaki, 2010), a meaningful neural code should trigger a distinct response in the downstream neural circuit. Third, the temporal code should have physiological significance and be utilized by the brain to inform behavioral choices (Miesenbock, 2011; Panzeri et al., 2017).

While many studies have identified temporal codes occurring in response to naturally occurring sensory stimuli (Panzeri et al., 2010; Uchida et al., 2014), relatively few studies have shown that induction of specific temporal codes alter the firing of target neural circuits or affect behavior. For instance, in olfactory sensory neurons in mammals, varying the timing of firing relative to other neurons or the sniff cycle impacts firing of downstream neurons (Haddad et al., 2013; Smear et al., 2011). However, other studies have found that temporal coding in olfactory, visual, and somatosensory systems had no effect on the activity of target neurons or behavioral readouts (Blumhagen et al., 2011; Histed and Maunsell, 2014; O'Connor et al., 2013). Thus, the functional relevance for temporal coding alone to represent information about the environment and internal states remains controversial. Moreover, the molecular mechanisms that underlie the generation of different temporal codes within a neural circuit are largely unknown.

Here, in the clock neuron network in *Drosophila*, we demonstrate the presence of naturally occurring temporal spiking patterns associated with daytime vs. nighttime and find that the cycling of these patterns depends on the core clock and *wide awake* (*wake*), a recently identified clock output gene required for circadian regulation of sleep (Liu et al., 2014). Using optogenetic approaches *in vivo*, we show that these distinct patterns of clock neuron firing, in the absence of changes in firing rate, serve as a temporal code to signify time-dependent arousal and directly impact sleep behavior. From a large-scale forward genetic screen, we identify the molecular mechanisms underlying the generation of these clock-dependent temporal codes. We then use electrophysiological and computational analyses to delineate the biophysical processes that rhythmically shape spike morphology and tune the firing patterns of these clock neurons. Remarkably, we demonstrate that the temporal spiking pattern alone drives neural plastic changes, which mediate the transformation of temporal codes in clock neurons to increased firing of a downstream arousal circuit. Together, our data demonstrate a causal role for temporal coding in behavior, which is mediated by a distinct form of synaptic plasticity specifically triggered by the pattern of neural spiking.

Results

Temporal regulation of sleep quality is dependent on CLOCK and WIDE AWAKE

The circadian regulation of physiology and behavior is achieved, in part, by modulating the excitability and activity of clock neurons (Cao and Nitabach, 2008; Flourakis et al., 2015; Liu et al., 1997; Liu et al., 2014). However, studies to date have focused on rate coding of clock neurons, and it is unclear whether the pattern or timing of clock neuron firing is

functionally relevant for behavior. To address this question, we focused on the circadian clock network in *Drosophila* and on the posterior dorsal neurons 1 (DN1p) cluster in particular; these cells have been implicated in regulating sleep/wake behavior (Guo et al., 2016; Kunst et al., 2014), and they directly project to a defined arousal circuit (Dilp2+ neurons of the pars intercerebralis) (Barber et al., 2016), thus allowing for detailed analyses of behavioral outputs and circuit signaling mechanisms.

In order to analyze temporal patterns of spike trains, we performed recordings of the DN1p neurons using perforated patch-clamp technique to enhance stability of the recordings by reducing "wash-out" of DN1p intracellular contents. DN1p neurons exhibited irregular firing during the mid-day (ZT6–8, Zeitgeber Time 6–8), but regular firing at mid-night (ZT18–20). This cycling of the regularity of spike firing was absent in the core clock mutant *Clk*[*jrk*] and with loss of *wake*, which we have previously shown impairs circadian-dependent cycling of clock neuron firing rate (Liu et al., 2014) (Figures 1A-1F, S Figure S1A-S Figure S1D and Table S1) (see STAR Methods for discussion of measures of irregularity). Strikingly, in contrast to the change in spike timing pattern, the spontaneous and evoked mean firing rates (MFR) of DN1ps did not differ between day (ZT6–8) and night (ZT18–20) (Figures 1C and SFigure S1E).

Because differences in spiking patterns of individual cells within the DN1p cluster could influence analyses of temporal coding, we performed dual patch-clamp recordings. We found clear evidence of both electrical coupling and spike timing synchronization between pairs of DN1p neurons (Figures SFigure S1F-SFigure S1H), suggesting that our recordings from single cells accurately reflect the spiking patterns of the group of neurons being studied. In addition, because bursting can represent a form of temporal coding, we asked whether bursting occurred in these neurons at mid-day vs mid-night. As shown in Figure SFigure S1I, bursting was not observed in DN1ps at ZT6–8 or ZT18–20, but was observed at ZT0–2. In contrast, bursting was observed in DN1ps at both ZT6–8 and ZT18–20 in *Clk* and *wake* mutants (Figure SFigure S1I), consistent with the notion that additional sleep/ wake phenotypes are observed in these mutants. We also assessed the relative contributions of synaptic vs intrinsic mechanisms underlying the generation of the regular nighttime spike train in the DN1ps (Figures SFigure S1J-SFigure S1N). Application of synaptic blockers did not significantly alter MFR or local (LV and CV_2) or global (CV) measures of irregularity, suggesting that CLK and WAKE-dependent generation of regular nighttime spike trains in these cells largely occurs in a cell-autonomous manner. Similar findings regarding the timing and rate of spike firing were obtained in another clock neuron cluster, the large ventrolateral neurons (l-LNvs) (Figures SFigure S2A-SFigure S2J). Thus, the *Drosophila* circadian network presented an unusual opportunity to dissect the role of intrinsic temporal spike patterns, uncoupled from rate coding, in behavior and synaptic signaling.

We next examined the relationship between this cycling pattern of spike timing and sleep behavior. Sleep amount did not differ between mid-day (ZT6–8) or mid-night (ZT18–20) periods in control flies. In contrast, sleep quality, as measured by sleep consolidation (sleep bout duration and number), brief awakenings, and arousal threshold, was greater during the night compared to the day (Figures 1G–1K, SFigure S2K). Similar findings were obtained under constant darkness conditions (D:D) (Figures SFigure S2L-SFigure S2P). This cycling

of sleep quality was dependent on both CLK and WAKE (Figures 1G–1K, SFigure S2K), indicating that it is under circadian control. Together, these data suggest that CLK- and WAKE-dependent temporal coding in the DN1ps is associated with cycling of sleep quality between the day and the night.

Optogenetic activation of DN1ps using different temporal spike patterns regulates sleep quality

To demonstrate that the different patterns of spike firing observed in the DN1ps directly control sleep quality, we developed an optogenetic/imaging preparation. In these assays, a single fly expressing CsChrimson (Klapoetke et al., 2014) in DN1ps is tethered and locomotor activity assessed using a frame subtraction method following optogenetic triggering of regular or irregular firing patterns (Figures 2A and2B). We first confirmed diurnal cycling of locomotor activity and validated the use of 5 min locomotor inactivity to identify sleep behavior in this preparation (Figures S3A and S3B). Wild-type flies, exposed to "sham" optogenetic stimulation, exhibited an increase in sleep quality, but not amount, at mid-night compared to mid-day in this assay (Figures S3F-S3K).

We next performed optogenetic manipulation of the DN1ps using irregular daytime and regular nighttime rate-matched temporal codes derived from actual patchclamp recordings of these cells ("playback") at ZT18–20 and found that irregular temporal spike patterns induced a decrease in sleep quality, compared to regular temporal spike patterns, without altering sleep amount (Figures S3L-S3Q). To confirm these findings, we wished to generate synthetic temporal codes which would allow for exact matching of firing rate. We thus performed mathematical modeling of our spike timing data by training a 5-component Gaussian mixture model (GMM) of second-order spike timing correlations on day (ZT6–8; Figures 2C and 2D) and night (ZT18–20; Figures 2F and 2G) datasets. To assess whether these synthetic spike patterns are biologically realistic, we generated a sample code from the GMM that was the same size as the training datasets and found that the synthetic temporal spike pattern precisely recapitulated the distribution of normalized spike timing from our DN1p recordings (Figures 2E and 2H). We then optogenetically activated DN1p neurons using these synthetic temporal codes at ZT18–20 and found, as expected, that the "day" temporal code induced reduced sleep quality, compared to the "night" temporal code, without affecting sleep amount (Figures 2I–2N).

Because precision of optogenetic control is important for assessing temporal coding, we first examined the correlation of spike firing in response to regular CsChrimson activation and found excellent fidelity at firing rates   6 Hz (Figures S3C and S3D). To directly compare the irregular CsChrimson-induced patterns with evoked spiking of the DN1ps, we performed simultaneous optogenetic activation of the synthetic irregular daytime pattern with perforated patch-clamp recordings of the DN1ps. As shown in Figure S3E, the latency between the optogenetic stimulus and the evoked DN1p spike was highly consistent (6.3 $\pm$ 0.5 ms). Moreover, global (CV) and local (CV_2 and LV) measures of irregularity for the two patterns were very similar (Figure S3E, inset). We next characterized the optogenetic and evoked spiking patterns at the level of individual spikes. Individual optogenetic stimuli were associated with a following DN1p spike 98.9% $\pm$ 2.1% of the time, while conversely,

each DN1p spike was associated with a preceding optogenetic stimulus 98.4% ± 4.9% of the time. Together, these data demonstrate a high degree of fidelity between the optogenetically-triggered patterns and the resulting DN1p spiking patterns. To confirm that the phenotypes observed with optogenetic activation of irregular temporal patterns localize to the DN1p neurons, we used an independent driver line that labels the DN1p neurons and obtained similar data (Figures S4A-S4G). We also asked whether local rate variations, rather than the irregularity, of the firing pattern influence sleep/wake states, and so we analyzed the data in Figure 2I and found no correlations between estimated MFR and awake, brief awakening, or sleep states (Figure S3R). Together, these data demonstrate that optogenetic triggering of specific temporal spike patterns in DN1ps is sufficient to determine sleep quality in behaving animals.

WAKE upregulates K_{Ca} current at night to enhance regularity of spike firing and sleep quality

To delineate the molecular mechanisms underlying the circadian-dependent temporal coding of sleep quality, we chose to use *wake* as a genetic entry point. Overexpression of *wake* in crustacean cardioactive peptide (CCAP) neurons (which are important for wing expansion) (Luan et al., 2006) resulted in unexpanded wings in ~70% of animals. To identify genes whose knockdown could suppress this WAKE-induced phenotype, we performed an RNAi screen of ~1,200 lines. From this screen, we identified the K_{Ca} channel Slowpoke (SLO) (Schopperle et al., 1998), its binding partner SLOB (Schopperle et al., 1998) and an uncharacterized Na^+/K^+ ATPase β subunit (CG33310, NaK β) as potential WAKE interactors (Figure 3A).

We first focused on the role of SLOB in WAKE-dependent temporal coding of sleep quality and began by investigating the WAKE and SLOB interaction. To address whether WAKE and SLOB biochemically interact, we co-expressed *wake-FLAG* and *slob-HA* in cultured HEK cells and found that SLOB co-immunoprecipitated with WAKE, suggesting that they physically interact in a complex (Figure S5A). SLOB has been shown to regulate the K_{Ca} channel SLO, which itself was a "hit" in our screen (Schopperle et al., 1998). Thus, we measured K_{Ca} current amplitude from DN1ps and found that it was significantly increased at night vs. the day. This cycling of K_{Ca} current amplitude was dependent on both WAKE and SLOB (Figures 3B–3D and S4H). Interestingly, increased K_{Ca} current leads to greater afterhyperpolarization (AHP) amplitude of spikes (Lancaster and Nicoll, 1987); AHP in turn has been proposed to be important for temporal coding (Goldberg et al., 1984; Piotrkiewicz, 1999). Thus, we performed spike waveform analysis of our current-clamp data and found that AHP amplitude was greater at night compared to the day in wild-type flies and that this cycling of AHP amplitude was lost in *Clk* mutants, *wake* mutants, and in flies with knockdown of SLOB in DN1ps (Figures 3E, 3F, and S4I, and Table S1). Similar data for WAKEdependent cycling of K_{Ca} and AHP amplitude were also obtained from l-LNv neurons (Figures S5B-S5F).

Modeling studies have suggested that greater AHP amplitude leads to more regular firing (Stiefel et al., 2013), so we examined DN1p temporal coding in flies with knockdown of SLOB in these cells. As shown in Figures 3G, 3H, and S4J, these flies lose cycling of the

regularity of spike timing, exhibiting irregular firing both during the day and the night. As expected, sleep quality at night vs. the day was reduced in flies with knockdown of SLOB in DN1ps, compared to controls, while sleep amount was unaffected (Figures 3I–3K, S4N-S4P, and S4T-S4V). These data suggest that WAKE acts via SLOB to enhance AHP amplitude and promote regular spike timing and greater sleep quality at night.

WAKE acts via a Na⁺/K⁺ ATPase subunit to increase spike onset rapidness and modulate spike timing and sleep behavior

We next investigated the role of NaKβ in regulation of temporal spike patterns and sleep. β -subunits are modulatory subunits of Na^+/K^+ ATPases that typically promote pump activity (Horisberger et al., 1991; Jaisser et al., 1994). Spike onset slope and precision (i.e., the consistency of spike onset slope time-to-peak) depend on Na^+/K^+ pump activity (Naundorf et al., 2006; Zhang et al., 2017), and so we examined spike onset slope dynamics in DN1ps. Spike onset rapidness was greater at night compared to day in wildtype flies, and this difference was lost in *Clk* mutants, *wake* mutants, and flies with knockdown of *NaKβ* in the DN1ps (Figures 4A, 4B, and S4K, and Table S1).

Previous computational work has shown that greater spike onset rapidness helps shape spike timing by enhancing spike onset precision (Ilin et al., 2013). Indeed, we found that spike onset precision, as measured by reliability, was greater at night vs. the day in controls, and this difference was attenuated in *Clk* mutants, *wake* mutants, and in flies with knockdown of *NaKβ* in DN1ps (Figures 4C and S4L). Similar data for CLK-, WAKE-, and NaKβ -dependent cycling of spike onset rapidness and precision were also obtained from l-LNvs (Figures S5G-S5I). We next examined whether NaKβ regulated temporal coding of sleep quality. Knockdown of NaKβ in DN1ps resulted in irregular spike firing during both the day and the night, in contrast to control flies, where regular firing was observed during the night (Figures 4D and S4M). Similarly, sleep quality at night resembles that seen during the day in these animals (Figures 4E–4G, S4Q-S4S, and S4W-S4Y).

We wished to perform computational modeling to address whether changes in K_{Ca} conductance (via SLOB) and Na^+/K^+ ATPase activity (via NaKβ) could reproduce the effects on spike-train variability and spike morphology seen with our experimental data. To do this, we extended a previous model of clock neuron activity based on diurnal shifts in Na⁺ and K⁺ leak conductances (Flourakis et al., 2015) (and see STAR Methods). To compare variability in the spiking outputs, we provided model neurons with a shared, stochastic, time-varying input current. Enhancing K_{Ca} current slowed firing during periods of high input, while increasing Na^+/K^+ ATPase activity maintained firing across pauses in the day spike train (Figure 4H). Each of these manipulations, but particularly when combined, improved regularity of the spike train (Figures 4H and 4I, S5J and S5K), similar to that seen in our experimental data at night. Interestingly, because of the opposing effects of K_{Ca} and Na^+/K^+ ATPase on firing rate, the implementation of both factors in the model resulted in a relatively neutral impact on mean firing rate (Figure S5K). To validate our model's predictions, we next analyzed the ISI distributions during the night from DN1ps in flies where SLOB or NaKβ were knocked down in these cells. These data reveal that knockdown of SLOB led to a shift towards shorter ISIs, whereas knockdown of NaKβ resulted in a shift

towards longer ISIs (Figure 4J); these experimental findings confirm our model's specific predictions regarding the effects of K_{Ca} current and Na$^+$/K$^+$ ATPase activity on spike timing.

Finally, we investigated whether our model recapitulated the effects of SLOB and NaKβ on spike morphology. Indeed, K_{Ca} and Na$^+$/K$^+$ ATPase modulation, both independently and in combination, deepened the average spike AHP and increased the maximum action-potential slope (Figures 4K and S5L), reminiscent of the spike morphology changes experimentally observed at night. Thus, K_{Ca} and Na$^+$/K$^+$ pump comodulation are sufficient to qualitatively explain experimentally observed timedependent changes in DN1p spike shape and regularity.

CLK and WAKE regulate subcellular localization of SLOB and NaKβ in a time-dependent manner

Our data suggest that the circadian clock acts via WAKE to regulate K_{Ca} current and Na$^+$/K$^+$ ATPase activity, in order to modulate spike biophysical properties and spike timing patterns in clock neurons to ultimately control sleep. What are the mechanisms by which WAKE regulates SLOB and NaKβ in this process? We previously showed that WAKE regulates targeting of the GABA$_A$ receptor RDL (Resistant to Dieldrin) in a timedependent manner (Liu et al., 2014). To address potential cycling of SLOB localization, we expressed SLOB-HA in l-LNvs in wild-type, *Clk,* or *wake* mutant backgrounds. We performed these experiments in the l-LNvs, as opposed to the DN1ps, because of our greater ability to assess subcellular localization in the larger l-LNvs. As shown in Figures 5A-5C, SLOB expression at the plasma membrane was significantly greater at night, compared to the day, and this effect was dependent on CLK and WAKE. We next asked whether NaKβ targeting was also dependent on WAKE. We thus similarly expressed NaKβ-myc in l-LNvs in wild-type, *Clk*, or *wake* mutant backgrounds. NaKβ levels at the plasma membrane were greater at night, compared to the day, in wildtype flies, and this difference depended on CLK and WAKE (Figures 5E-5G). As shown in Figures 5D and 5H, loss of CLK and WAKE was also generally associated with a reduction in total levels of SLOB and NaKβ which may reflect increased degradation secondary to mis-targeting of these proteins. Taken together with our previous work (Liu et al., 2014), these data suggest that WAKE is a crucial clock output molecule for sleep behavior that broadly regulates multiple ion channels and pumps in a time-dependent manner by controlling the targeting of the channels themselves or their regulatory partners. While our WAKE/SLOB co-immunoprecipitation data (Figure S5A) suggest that WAKE directly regulates these channels and transporters, we cannot exclude an indirect effect secondary to alteration of neuronal excitability.

NMDA receptor signaling in arousal-promoting Dilp2+ PI neurons enhances sleep quality

What are the circuit mechanisms by which the diurnal cycling of temporal spike patterns of DN1ps leads to changes in sleep behavior? The DN1p neurons project directly to arousal-promoting non-clock neurons, the Dilp2+ (*Drosophila* insulin-like peptide2) PI neurons (Barber et al., 2016). Recent work has shown that the mean firing rates (MFR) of these Dilp2+ PI neurons cycles, with greater firing rates during the day, compared to the night (Barber et al., 2016). We reproduced these findings by performing perforated patch-clamp recordings of Dilp2+ PI neurons at mid-day and mid-night. These neurons exhibit a marked

difference in firing rate at these time windows, with almost no firing at night, and this cycling of MFR was dependent on WAKE (Figures S6A-S6D). Given these findings, we hypothesized that temporal coding in DN1ps is transformed into rate coding changes in the Dilp2+ PI neurons and that Ca^{2+} signaling, which is instrumental in integrating temporal signals (Ghosh and Greenberg, 1995), is involved in this process.

To identify the molecular mechanisms involved in this transformation of temporal coding to rate coding, we performed a targeted RNAi screen of Ca^{2+}-related signaling molecules in the downstream Dilp2+ PI neurons. We assessed changes in the cycling of daytime vs. nighttime sleep quality by calculating the ratio of sleep bout duration during ZT6–8 vs. ZT18–20. Knockdown of the 2 subunits of the NMDA receptor (dNR1 and dNR2) (Wu et al., 2007) led to the greatest increase in the ratio of day to night sleep bout duration (Figure 6A). As shown in Figures 6B-6I, flies with knockdown of dNR1 or dNR2 in the Dilp2+ PI neurons lost the diurnal cycling of sleep quality and exhibited reduced nighttime sleep quality. These data suggest that NMDA receptor signaling in the PI neurons is important for promoting sleep quality at night.

The daytime temporal spike pattern drives synaptic plastic changes to effectuate rate coding changes and regulate sleep behavior

We next examined the effects of the different DN1p temporal spike patterns on Dilp2+ PI neuron activity. To do this, we performed *in vivo* intracellular current-clamp recordings of the Dilp2+ PI neurons while simultaneously optogenetically activating the DN1ps using different temporal codes (Figure 7A). The MFR of the Dilp2+ PI neurons was not appreciably different when triggering regular firing of the DN1ps using "night" synthetic temporal spike patterns (Figures 7B and 7D). Strikingly, however, optogenetic activation of DN1ps using rate-matched irregular "day" synthetic temporal spike patterns led to a significant increase in Dilp2+ PI neuron MFR (Figures 7B and 7C). This potentiation of Dilp2+ PI neuron firing exhibited substantial latency (i.e., required about 5 min of the irregular temporal spike pattern) and persisted following cessation of the optogenetic activation. This effect was also dependent on NMDA receptor signaling, as it was abolished with knockdown of dNR1 in these cells (Figures 7B and 7E). It is worth noting that, given the substantial difference between their firing rates, it is unlikely that DN1p spikes directly trigger firing of the Dilp2+ PI neurons, but instead serve to drive potentiation of these synapses. We thus also examined whether spike onset threshold, resting membrane potential, or membrane potential fluctuations in the Dilp2+ PI neurons were altered after potentiation and found that these cells exhibit a significant increase in membrane potential fluctuations (Figure S6I-S6K).

One of the challenges of studying the function of temporal pattern codes, as distinct from rate codes, is that if shorter time windows are considered for an irregular pattern, specific time windows can be identified with an increase in "firing rate" (i.e., brief fast spiking intervals). These brief fast spiking intervals (typically <90 ms) could thus represent a hidden rate code within a purported temporal pattern code. To address whether such brief fast spiking intervals are important for DN1p-Dilp2+ PI neuron signaling, we first determined the minimum time window length that would faithfully reproduce the MFR of the entire

spike train. To do this, we analyzed sliding time windows of different durations for our synthetic daytime spike trains and determined that a 40 sec window (and all longer windows) was sufficient to consistently maintain an MFR similar to that for the entire spike train (Figure S6E, and see STAR Methods). As shown in Figures S6F and S6G, optogenetic activation of the DN1ps using a 40 sec window of the irregular daytime synthetic code did not induce an appreciable change in Dilp2+ PI neuron MFR. These data suggest that the brief fast spiking intervals found within a 40 sec window are not sufficient for driving potentiation of the Dilp2+ PI neurons and instead argue that persistence of the "day" temporal pattern of DN1p neuron spiking is required.

To investigate the mechanisms underlying these neural plastic changes, we next characterized synaptic properties following optogenetic activation with "day" vs. "night" temporal codes. The frequency of Dilp2+ PI neuron excitatory post-synaptic potentials (EPSPs) was similar when triggering DN1 firing using "day" temporal codes in the presence or absence of dNR1 knockdown or "night" temporal codes (Figure 7N). In contrast, the slope and amplitude of these EPSPs were significantly increased when "day" synthetic temporal spike patterns were used to optogenetically activate the DN1ps, compared to rate-matched "night" temporal spike patterns, and this effect was suppressed with knockdown of dNR1 in these cells (Figures 7F-7M). These changes in EPSP slope and amplitude in the Dilp2+ PI neurons suggest that post-synaptic plastic processes drive the increase in their firing in response to "day" temporal codes, although non-synaptic plasticity mechanisms cannot be excluded.

Our data suggest that the observed DN1p-PI synaptic plasticity depends upon the pattern, but not the rate, of DN1p spiking. While the timing of spiking has been shown to influence plasticity (Kumar and Mehta, 2011), our findings, to our knowledge, describe one of the first examples of synaptic plasticity being triggered by changes in the regularity of presynaptic spiking. To further support this notion, we assessed whether the plasticity observed at DN1p-PI synapses simply reflects underlying spike-timing dependent plasticity (STDP). We examined the relative spike timing of the DN1p and Dilp2+ PI neurons and did not identify a noticeable peak in the relative spike timing distribution (Figure S6H), making it unlikely that STDP underlies the plastic changes in the PI neurons. Together, these data demonstrate that daytime temporal codes in the DN1p neurons are transformed into rate coding changes in the arousal-promoting Dilp2+ PI neurons via NMDA receptor-dependent post-synaptic plastic changes, to modulate sleep quality (Figure 7O).

Discussion

The molecular mechanisms underlying the generation of different temporal codes are largely unknown. Here, we show that the circadian clock drives distinct temporal spiking patterns, as defined by the second-order temporal structure of interspike intervals, by adjusting ionic flux in clock neurons in a time-dependent manner. These changes are mediated by the clock output molecule WAKE, which controls the membrane targeting of SLOB and a Na^+/K^+ ATPase β subunit. This dynamic regulation of ionic flux leads to cycling of specific aspects of spike waveforms, which in turn induces the temporal spiking patterns seen during the day vs. the night.

From a broader perspective, our work addresses a central issue in neuroscience: the functional importance of temporal codes in encoding information and impacting behavior. One challenge in demonstrating a causal role of temporal coding is identifying systems with a defined neural circuit where changes in the pattern or timing of spiking occur naturally, lead to measurable effects in target neurons, and regulate a specific behavior. An additional confounding factor is that information can be coded in a multiplexed manner, with concurrent spatial, temporal, and rate-related features (Panzeri et al., 2010). Here, we show that the *Drosophila* clock network fulfill these criteria and find that time is encoded unidimensionally by the spiking patterns of these neurons, in the absence of changes in firing rate or network timing (due to synchronization of neural firing within a cluster). Moreover, using computational, *in vivo* optogenetic, and electrophysiological approaches in these clock neurons, we demonstrate this temporal coding has functional consequences on the firing of a target arousal circuit and on sleep behavior. While our findings suggest that the irregular 2nd order spiking pattern is critical for this process, it is also possible the temporal code consists of brief periods of faster spiking that are repeated over a >40s timeframe.

We previously demonstrated that WAKE is critical for clock-dependent regulation of sleep onset at dusk and that it upregulates $GABA_A$ receptor levels and targeting to mediate this process by markedly suppressing the firing rate of clock neurons (Liu et al., 2014). Why would multiple neural coding mechanisms (rate coding changes at dusk and temporal coding at mid-day and mid-night) evolve to underlie circadian clock regulation of sleep at different times? One possibility relates to the dynamics of sleep onset versus sleep quality. Transitions between sleep and wake are major changes in brain state occurring on a relatively short timescale and hence may require dramatic changes in firing rate (i.e., rate coding) that are energetically costly (Levy and Baxter, 1996; Harris et al., 2012). In contrast, maintenance of sleep quality occurs over hours; thus, it may be more energetically favorable for the relevant neurons to alter the pattern, instead of the rate, of their firing. Because of these potential energy savings, we speculate that the use of temporal spiking patterns to encode information could be a broadly used mechanism for representing persistent internal states, such as hunger or emotion.

Finally, we demonstrate that changes in the pattern of spike firing in the DN1ps, independent of changes in firing rate, triggers NMDA-receptor dependent post-synaptic plasticity in the Dilp2+ PI neurons. Importantly, these data suggest a specific mechanism for inducing synaptic plasticity, distinct from previously described processes that are dependent on changes in rate coding (e.g, long-term potentiation) (Bailey et al., 2000) or relative timing of individual spike events (e.g., spike-timing dependent plasticity) (Markram et al., 1997). To our knowledge, these data represent one of the first examples of synaptic plasticity being induced specifically by the intrinsic temporal pattern of spiking, expanding the repertoire by which neural codes can generate plasticity. Together, our findings suggest that temporal patterns of spike firing are a crucial mechanism for driving neural plastic changes that mediate how internal states modulate behavior.

STAR METHODS

KEY RESOURCES TABLE

REAGENT or RESOURCE	SOURCE	IDENTIFIER
Antibodies		
Normal goat serum	JacksonImmunoresearch	Cat#005–000-121
rabbit anti-FLAG	MilliporeSigma	Cat#F7425; RRID: AB_439687
rat anti-HA	Roche	Cat#3F10; RRID: AB_2314622
rat anti-WAKE-Ab2	Wu Lab	N/A
rat anti-GFP	Santa Cruz	Cat#101536; RRID: AB_1124404
Rabbit anti-GFP	Thermo Fisher	Cat#A-11122; RRID: AB_221569
goat anti-rat HRP	Thermo Fisher	Cat#31470; RRID: AB_228356
mouse anti-MYC	Developmental Studies Hybridoma Bank	Cat#9E10; RRID: AB_2266850
Mouse anti-BRP	Developmental Studies Hybridoma Bank	Cat#nc82; RRID: AB_2314866
Goat anti-rat IgG, Alexa488	Thermo Fisher	Cat#A-11006; RRID: AB_2534074
Goat anti-mouse IgG, Alexa488	Thermo Fisher	Cat#A32723; RRID: AB_2633275
Goat anti-rabbit IgG, Alexa488	Thermo Fisher	Cat#A27034; RRID: AB_2536097
Goat anti-mouse IgG, Alexa568	Thermo Fisher	Cat#A-11004; RRID: AB_141371
Bacterial Strains		
Top10	Thermo Fisher	Cat#C404003
Chemicals, Peptides, and Recombinant Proteins		
Dulbecco's Modified Eagle Media	Thermo Fisher	Cat#11965–092
L-glutamine	Thermo Fisher	Cat#25030081
Fetal bovine serum	Thermo Fisher	Cat#16140071
Penicillin-Streptomycin	Thermo Fisher	Cat#15140122
Effectene Transfection Reagent	Qiagen	Cat#301425
0.5x RIPA Buffer	MilliporeSigma	Cat#R0278
Protein G-coated magnetic	Thermo Fisher	Cat#1003D
Dynabeads		
Pierce ECL Western Blotting Substrate	MilliporeSigma	Cat#32016
DAPI	MilliporeSigma	Cat#10236276001
Paraformaldehyde, EM grade	Polysciences, Inc.	Cat#00380–250
all-trans-retinal	MilliporeSigma	Cat#R2500
Nutri-Fly Instant food flakes	Genesee Scientific	Cat#66–117
Neurobiotin	Vector Labs	Cat#SP-1120
Picrotoxin	MilliporeSigma	Cat#P1675
Mecamylamine HCl	Tocris Bioscience	Cat#2843
Escin	Santa Cruz	Cat#SC-221596
Collagenase	MilliporeSigma	Cat#C5138
Protease XIV	MilliporeSigma	Cat#P5147

REAGENT or RESOURCE	SOURCE	IDENTIFIER
Dispase	MilliporeSigma	Cat#04942078001
Streptavidin, Alexa488-conjugate	Thermo Fisher	Cat#S11223
Streptavidin, Alexa568-conjugated	Thermo Fisher	Cat#S11226
4-Aminopyridine	MilliporeSigma	Cat#A78403
Tetrodotoxin	Tocris Bioscience	Cat#1078
Cadmium chloride	MilliporeSigma	Cat#655198
Experimental Models: Cell Lines		
HEK293T	American Type Culture Collection	Cat#CRL-3216; RRID: CVCL_0063
Experimental Models: Organisms/Strains		
wake-GAL4	Wu Lab	N/A
UAS-CD8::GFP	Bloomington Drosophila Stock Center	BDSC: 5137
wake^{D2}	Wu Lab	N/A
Clk^{jrk}	Bloomington Drosophila Stock Center	BDSC: 24515
PDF-GAL4	Bloomington Drosophila Stock Center	BDSC: 6900
R18H11-GAL4	Bloomington Drosophila Stock Center	BDSC: 48832
R18H11-LexA	Bloomington Drosophila Stock Center	BDSC: 52535
Clk4.1m-GAL4	Bloomington Drosophila Stock Center	BDSC: 36316
20xUAS-IVS-GCaMP6s	Bloomington Drosophila Stock Center	BDSC: 42749
10xUAS-IVS-myr::tdTomato	Bloomington Drosophila Stock Center	BDSC: 32222
13xLexAop2_IVS-CsChrimson.mVenus	Bloomington Drosophila Stock Center	BDSC: 55139
20xUAS-IVS-CsChrimson.mVenus	Bloomington Drosophila Stock Center	BDSC: 55135
CCAP-GAL4	Bloomington Drosophila Stock Center	BDSC: 25686
UAS-slob-HA	FlyORF	FlyORF: F003557
UAS-slob RNAi	Vienna Drosophila Research Center	VDRC: 100987
UAS-slob RNAi #2	Vienna Drosophila Research Center	VDRC: 30674

REAGENT or RESOURCE	SOURCE	IDENTIFIER
UAS-NaKβ RNAi	Vienna Drosophila Research Center	BDRC: 105863
UAS-NaKβ RNAi #2	Vienna Drosophila Research Center	VDRC: 48300
UAS-dsNR1 RNAi	C.-L. Wu	N/A
UAS-dsNR2 RNAi	C.-L. Wu	N/A
dilp2-GAL4	A. Sehgal	N/A
dilp2-mCherry	A. Sehgal	N/A
UAS-wake	Wu Lab	N/A
Recombinant DNA		
pUAS-NaKβ-myc	Wu Lab	N/A
pUAST-6xmyc	Wu Lab	N/A
pUAST-WAKE-T-Flag	Wu Lab	N/A
pCMV-Slob65-HA	I. Levitan	N/A
pCMV-actin-GAL4	Wu Lab	N/A
pCMV-eGFP	Wu Lab	N/A
Oligonucleotides		
GGCGCGGCCGCATGTCGG ACGATGATAAAAATC	MilliporeSigma	N/A
GCCCTCGAGTAATGAGTA GTCGGTTCGGAGTAATTTTTC	MilliporeSigma	N/A
Software and Algorithms		
MATLAB R2017b	Mathworks	RRID: SCR_001622
Fiji (ImageJ)	NIH	RRID: SCR_002285
pClamp 10.3	Molecular Devices	RRID: SCR_011323
Prism 6	GraphPad	SCR_002798
Other		
Dental wax	GC Corporation	Cat#27B2X00008000016
Vectashield	Vector Labs	Cat#H-1000
fiber optic cannula	Thorlabs	Cat#CFML21L10
Arduino Uno board	Arduino	Cat#A000066
collimated LED light source (625nm)	Thorlabs	Cat#M625F2
quartz glass with filament (OD/ID: 1.2/0.6mm)	Sutter Instruments	Cat#QF120–60-7.5
Borosilicate glass (OD/ID: 1.2/0.68mm)	A-M Systems	Cat#627500
syringe filter with 0.02μm pore size, Anotop10	Thermo Fisher	Cat#09–926-3

CONTACT FOR REAGENT AND RESOURCE SHARING

Further information and requests for resources and reagents should be directed to and will be fulfilled by the Lead Contact, M.N. Wu (marknwu@jhmi.edu).

EXPERIMENTAL MODEL AND SUBJECT DETAILS

Drosophila—All fly lines used, including GAL4 and UAS transgenic lines, were generated in the *iso*[31] background or outcrossed into the *iso*[31] genetic background at least 5 times.

Flies were reared on standard food containing molasses, cornmeal, and yeast at room temperature or 25°C. 4–8 day old female flies were used for all experiments. Transgenic animals were generated using standard techniques (Rainbow Transgenics). We used two different GAL4 drivers to label and manipulate the DN1p neurons. *R18H11-GAL4* labels ~6 DN1p neurons, and also exhibits expression in a few cells in the lateral brain, as well as the thoracic ganglia (Kunst et al., 2014 and see HHMI Janelia Flylight project http://flweb.janelia.org/cgi-bin/flew.cgi*). Clk4.1m-GAL4* specifically labels ~8–10 DN1p neurons in the central brain (Zhang et al., 2010a; Zhang et al, 2010b) and labels only 4 cells in the thoracic ganglion (see Figure S4A)

HEK293T Cells—*HEK293T* cells (female origin) (ATCC) were cultured in Dulbecco's Modified Eagle Media (Thermo Fisher) with 2 nM L-glutamine (Thermo Fisher), 10% fetal bovine serum (FBS) (Thermo Fisher), and 100 units/ml of Penicillin-Streptomycin (Thermo Fisher). Cells were grown to ~80% confluency in culture flasks in an incubator at 37°C, with 95% O_2 and 5% CO_2. Experiments using cultured cells were performed using cells passaged 7 or fewer times, and fresh media was made each week.

METHOD DETAILS

Molecular Biology—To generate *UAS-NaKβ-myc*, the *UAS-NaKβ/CG33310* open reading frame was PCR amplified using the following primers: 5'- GGC GCG GCC GCA TGT CGG ACG ATG ATA AAA ATC- 3' and 5'- GCC CTC GAG TAA TGA GTA GTC GGT TCG GAG TAA TTT TTC –3' and then digested with NotI and XhoI and subcloned into *pUAST6xmyc*. For the co-immunoprecipitation experiments, we used *pUAST-WAKE-T-Flag* (Liu et al., 2014) and *pCMV-Slob65-HA* (Jaramillo et al., 2006), which were previously described.

Co-immunoprecipitation—*pUAST-WAKE-T-FLAG*, *pCMV-Slob-HA*, *pCMV-actin-GAL4*, and/or *pCMV-eGFP* (as a negative control) were co-transfected singly or in combination into HEK293T cells using Effectene Transfection Reagent (Qiagen). Cells were harvested, and total protein extracted using 0.5x RIPA Buffer (MilliporeSigma) with 1 mM PMSF and 0.5 mM DTT. Rabbit anti-FLAG antibodies (MilliporeSigma) were bound to Protein G-coated magnetic Dynabeads (Thermo Fisher) overnight and then mixed with cell extracts for 2 hr with shaking at 4˚C. Beads were magnetically collected and then washed 4 times with extraction buffer. Immunoprecipitates were analyzed by Western blotting, using rat antiHA (1:2000, Roche), rat anti-WAKE-Ab2 (1:2000); rat anti-GFP (1:2000, Santa Cruz) in blocking solution (PBST with 5% nonfat powdered milk) overnight at 4˚C. Bands were visualized by enhanced chemiluminescence following 2 hr incubation at RT with goat anti-rat HRP secondary antibodies (1:10,000).

wake genetic interaction screen—Expression of WAKE in CCAP (crustacean cardioactive peptide) neurons, which are required for wing expansion (Luan et al., 2006), results in unexpanded wings in ~70% of flies, likely due to alterations in excitability. To identify novel WAKE interactors, we conducted an RNAi screen to find suppressors of this phenotype, by crossing *CCAPGAL4>UAS-wake* flies to 1,167 different RNAi lines and examining wing expansion of their progeny. We scored wing phenotypes as either fully

expanded or unexpanded (which included partially expanded), and calculated a rescue index based on the % unexpanded wings (UE%) relative to the index line *CCAP-GAL4>UAS-wake* (70% - UE% / 70%).

Immunostaining and subcellular localization—Brains or thoracic ganglion were fixed in 4% PFA for 30 mins at room temperature. After several washes with phosphate-buffered saline (137 mM NaCl, 2.7 mM KCl, 10 mM Na_2HPO_4, 1.7 mM KH_2PO_4) + 0.3% Triton X-100 (PBST), samples were incubated with rat anti-HA at 1:100 (3F10, Roche) mouse anti-MYC (9E10, Developmental Studies Hybridoma Bank) at 1:50, rabbit anti-GFP (Thermo Fisher), and/or mouse anti-BRP (nc82, Developmental Studies Hybridoma Bank) at 4°C overnight. After additional PBST washes, samples were incubated with DAPI (Millipore Sigma, 1:1000) and/or Alexa488 anti-rabbit (Thermo Fisher, 1:1000) for anti-GFP stainings, Alexa568 anti-mouse (Thermo Fisher, 1:1000) for anti-BRP stainings, Alexa488 anti-rat (Thermo Fisher, 1:1000) for anti-HA stainings or Alexa488 anti-mouse (Thermo Fisher, 1:1000) for antimyc stainings overnight at 4°C. For stainings using the *Clk4.1m-GAL4* driver, images were taken under 25x magnification using a Zeiss LSM700 and acquired as 512×512 pixel images. For subcellular localization experiments, images were taken under $63\times$ magnification using a Zeiss LSM700 and acquired as $1,024 \times 1,024$ pixel images. The 1 μm slice with the strongest nuclear DAPI signal was used to quantify the appropriate region of interest (ROI) from each cell. ImageJ was used to quantify intensity of total, plasma membrane, and perinuclear signal. Analysis of SLOB-HA and NaKβ−myc localization (Figure 5) was performed in the l-LNvs, instead of the DN1ps, because changes in subcellular localization were more easily visualized in the former cells, which are larger.

Sleep Analysis

Standard beam-break analyses: Sleep behavior was measured using consolidated locomotor inactivity as previously described (Liu et al., 2014). Females were loaded into glass tubes containing 5% sucrose/2% agarose and were then monitored using the *Drosophila* Activity Monitoring System (Trikinetics) under 12 hr:12 hr light:dark (LD) or dark:dark (DD) conditions. Activity counts were collected in 1 min bins, and sleep was identified as periods of inactivity lasting at least 5 minutes. Brief awakenings were calculated essentially as previously described, as a single 1 min bin with either 1 or 2 beam crossings, flanked by 1 min bins with no locomotor activity (Huber et al., 2004). Sleep bout durations were calculated for the 2 hr windows; thus the maximum sleep bout duration possible was 2 hrs.

Single fly video analyses: For experiments involving simultaneous measurement of sleep behavior with optogenetic manipulation, individual flies were anesthetized on ice and glued to a 0.025 mm thick stainless steel shim using dental wax. Flies were given ad libitum access to food (rehydrated food flakes, Nutri-Fly Instant, Genesee Scientific), and leg movements were continuously monitored with an IR-sensitive CCD camera (Ailipu Technology) at 2 fps. Inactivity assessed by leg movements was transformed to sleep behavior via a frame-subtraction approach using a noise threshold algorithm, as previously described (van Alphen et al., 2013). Sleep was identified using a 5 min window for this assay was validated by arousal threshold criteria, as determined by administration of varying

strengths of air puffs (Figure S3B). Brief awakenings were calculated by detecting "010" sequences (1 = active, 0 = inactive) in the 1 min binned data, where an "active" bin was defined by the presence of any pixel change beyond a 2 SD threshold (van Alphen et al., 2013). 90 min of recording data were used for these analyses, because the first 30 mins of the 2 hr window were used to allow the fly to acclimate to the preparation.

Optogenetic stimulation

Flies were fed 1 mM all-trans-retinal (MilliporeSigma), mixed in rehydrated food flakes (Nutri-Fly Instant, Genesee Scientific). A collimated LED light source (625nm, Thorlabs) was used for photostimulation of CsChrimson-expressing DN1p cells. A fiber optic cannula (Thorlabs) was attached to the LED to converge the light. An Arduino Uno board (Arduino) was connected to a computer running MATLAB and used to control the timing of photostimulation. For optogenetic activation of DN1ps using the shorter time window, 40 sec windows from 3 of the synthetic daytime spike trains used in Figure 7B were selected. Because our data suggest that the DN1ps are gap junction-coupled (see Figures SFigure S1F-SFigure S1H), the degree of synchrony of DN1p firing under natural conditions vs triggered by optogenetic methods is likely highly similar, although it remains possible that greater synchrony is observed with optogenetic activation.

Electrophysiological recordings

***ex vivo* preparation:** Brains were removed and dissected in a *Drosophila* physiological saline solution (101 mM NaCl, 3 mM KCl, 1 mM $CaCl_2$, 4 mM $MgCl_2$, 1.25 mM NaH_2PO_4, 20.7 mM $NaHCO_3$, and 5 mM glucose; pH 7.2). To better visualize the recording site and increase the likelihood of a successful recording, the glial sheath surrounding the brain was focally and carefully removed after treating with an enzymatic cocktail, collagenase (0.2 mg/ml), protease XIV (0.4 mg/ml), and dispase (0.6 mg/ml), at 22°C for 1–2 min. The surface of the cell body was briefly cleaned with a small stream of saline that was pressure-ejected from a large-diameter pipette under visualization of a dissecting microscope. The brain was immobilized on the bottom of a recording chamber using a custom-made platinum anchor.

***in vivo* preparation:** Flies were mounted as described for single fly video analyses. Then, the cuticle was peeled off to expose the surface of the brain, and the tethered fly was mounted in a chamber containing a *Drosophila* physiological saline solution. The chamber was placed on the stage of an Olympus BX51 microscope, and the PI neurons were first visualized with mCherry or GCaMP6 fluorescence viewed with a 40× water immersion objective lens and then via infrared-differential interference contrast (IR-DIC) optics and a CCD camera (CV-A50IR; JAI, Japan).

Perforated patch-clamp recordings: Perforated patch-clamp recordings of l-LNv and DN1p neurons were performed essentially as described (Liu et al., 2016). The use of perforated, as opposed to whole-cell, patch-clamp configuration was important for analysis of temporal coding, because firing patterns recorded were more stable, likely due to reduced cell/electrode solution exchange. Fluorescently labelled neurons were visualized on a fixed-stage upright microscope (BX51WI, Olympus). The cell surface was further cleaned by

positive pressure from the recording electrode under visualization of a 40x objective lens before recording (Liu et al., 2016).

Escin was prepared as a 50 mM stock solution in water (stored up to 2 weeks at −20°C) and was added fresh into the internal pipette solution to a final concentration of 50 μM. Because escin is light-sensitive, filling syringes were wrapped with aluminum foil. Pipette tips were dipped briefly for 1 sec or less into a small container with escinfree internal pipette solution, and then were back-filled with the escin-containing solution from the filling syringe. Air bubbles were removed by gentle tapping. Escin pipette solutions remained stable for several hrs after mixing in the filling syringe, with no evidence of precipitate formation. Recordings were acquired with an Axopatch 200B amplifier (Molecular Devices) or a Model 2400 amplifier with 100 MΩ headstage (A-M systems), and sampled with Digidata 1440A interface (Molecular Devices). These devices were controlled on a computer using pCLAMP 10.3 software (Molecular Devices). The signals were sampled at 20 kHz and low-pass filtered at 2 kHz. Junction potentials were nullified prior to high-resistance (GΩ) seal formation. After establishing a GΩ seal, perforated patches were allowed to develop spontaneously over time (usually ~1–8 min) without any suction pulse applied in the pipette. After breakthrough became evident, as determined by the gradual development of a large capacitance transient in the seal test window of pCLAMP 10 software, access resistance monitoring was initiated employing the membrane test function. After that point, access resistance was monitored continuously during the final completion of perforation process, until it reached a minimal "steady state" (access resistance stably < 40 MΩ). Cells showing evidence of "mechanical" breakthrough, as assessed by the abrupt generation of a large capacitance transient (versus the more progressive, gradual one generated by chemical perforation), were excluded. In addition, cells were also excluded if "inflowing" cytosolic fluorescence into the pipette was visually detected during or after recording. One neuron per brain was recorded. During the recording, the bath solution was continuously perfused with saline by means of a gravity-driven system. Patch pipettes (8–10 MΩ) for perforated patch-clmap were fashioned from borosilicate glass capillary (without filament) using a Flaming-Brown puller (P-1000, Sutter Instrument) and further polished with a MF200 microforge (WPI) prior to filling internal pipette solution (102 mM potassium gluconate, 0.085 mM $CaCl_2$, 0.94 mM EGTA, 8.5 mM HEPES, 4 mM MgATP, 0.5mM Na-GTP, 17 mM NaCl; pH7.2). For experiments utilizing synaptic blockers, 50 μM mecamylamine and 250 μM picrotoxin were used to isolate the cells from most excitatory and inhibitory inputs; cells were recorded for 20 sec baseline ("control"), followed by 20 sec of application of synaptic blockers by gravity perfusion, and then 20 sec of recording for the "+ synaptic blockers" condition.

Ca^{2+}-dependent K^+ (K_{Ca}) currents were pharmacologically isolated with a combination of blockers, appropriate voltage protocols, and ion substitution, as previously described (Tabuchi et al., 2015). Specifically, neurons were held at −70 mV and two series of 200 ms voltage pulses were delivered in 10 mV increments between −80 mV and 60 mV in the presence of 1×10^{-7} M tetrodotoxin and 4×10^{-3} M 4aminopyridine. The second series was recorded additionally with saline containing 5×10^{-4} M $CdCl_2$, which abolished voltage-activated Ca^{2+} currents. The subtracted "Cd^{2+}treated" current series from the untreated current series was defined as K_{Ca} current.

For the optogenetic/DN1p spiking fidelity experiments, perforated patch-clamp recordings were conducted as above *for R18H11-GAL4>UAS-CsChrimson* flies, while simultaneously performing optogenetic activation as described above using irregular daytime (CV=1.2) synthetic temporal codes.

Dual recordings of DN1p neurons: Dual recordings from pairs of DN1p neurons were performed using two patch-clamp amplifiers-- an Axopatch 200B amplifier (Molecular Devices) and a Model 2400 amplifier with 100 MΩ headstage (A-M systems). To examine potential electrical coupling between DN1p cells, hyperpolarizing and subthreshold depolarizing current injections were applied to presynaptic cells, and the membrane potentials of non-injected postsynaptic cells were simultaneously recorded. Electrical coupling recordings were averaged across 30 trials, and the coupling coefficient between two DN1p cells was determined by the ratio of the voltage response in the postsynaptic cell divided by the voltage response in the presynaptic cell under steady-state conditions. The degree of spike-timing correlation of spontaneous activity of two DN1p cells was quantified by computing the cross-correlation function, which represents the probability of encountering a spike in one cell as a function of time before or after a spike in the other cell. Cross-correlograms were normalized by creating shuffled spike trains for each recording and subtracting the mean shuffled cross-correlogram from the raw mean cross-correlogram and then dividing by the standard deviation of the mean shuffled cross-correlogram. The cross-correlation function demonstrates a large peak around 0 ms, suggesting the presence of gap junctional connections between DN1p cells.

***In vivo* intracellular recordings:** Sharp electrode intracellular (as opposed to patch-clamp) recordings of Dilp2+ pars intercerebralis (PI) neurons were performed in order to clearly dissociate action potential spikes from excitatory post-synaptic potentials (EPSPs). These intracellular recordings were performed essentially as described (Liu et al., 2017), with modifications to enhance signal to noise and stability of the recordings. Sharp electrodes from quartz glass with a filament (OD/ID: 1.2/0.6mm) were fabricated with a laser-based micropipette puller (P-2000, Sutter instrument) and backfilled with 1% Neurobiotin dissolved in 1 M KCl, with resistances of 90–170 MΩ. Solutions were filtered by using a syringe filter with 0.02μm pore size (Anotop 10, Whatman). The electrode was inserted into the PI neurons expressing mCherry or GCaMP6 (for visualization). Signals were acquired with an Axoclamp 900A, and sampled with an interface, controlled by pCLAMP 10 software. The signals were sampled at 20 kHz and low-pass filtered at 2 kHz. In all cases, one neuron per brain was recorded, and we conducted post-hoc single cell staining, to confirm the identity of the recorded cell; data were included only if the cells were positively identified as PI neurons. The duration of the *in vivo* recordings ranged from 11 to 30 mins (mean = 19 mins). In all cases, potentiation of Dilp2+ PI neurons shown in Figure 7 lasted for as long as the recordings could be maintained.

Single-cell labeling: For intracellular recordings, single-cell labeling was performed by immunostaining of whole-mount brains as previously described (Liu et al., 2017). Intracellular staining was performed by iontophoretic injection of neurobiotin (1.2 nA depolarizing current, 500 ms duration, 1 Hz) for at least 10 min. Brains were then fixed in

4% paraformaldehyde in PBS overnight at 4°C. After several washes in PBST at room temperature over 1 hr, brains were incubated with Alexa488- or Alex568-conjugated streptavidin (Thermo Fisher, 1:100) for 24–40 hrs on a shaker at 4°C. After another series of washes in PBST at room temperature over 1 hr, samples were cleared in 70% glycerol in PBS for 5 min at room temperature and then mounted in Vectashield (Vector Labs). Brains were imaged as described in the Immunostaining section. Only samples where a single cell was both GFP-positive and dye-labeled were included in the analyses.

Synthetic stimulus patterns

For each dataset, ISIs (day, n=1847; night, n=2098) were normalized by cell-average firing rates and pooled across cells. Second-order distributions were created by logarithmic binning of adjacent pairs of normalized intervals into a 2D histogram (22×22 bins; day, natural log range [–2.225, 1.4]; night, [–0.415, 0.555]). Using a Gaussian mixture model (scikit-learn version 0.19.1), we fit 5 Gaussian components with full covariance to the joint second-order distributions; using fewer components did not capture the visually inspected statistical modes of the data. For validation, size-matched random samples from the model produced joint and marginal distributions that were indistinguishable from the training data. To generate a rate-matched pair of day/night stimulus patterns, we first sampled an average firing rate from a beta distribution fit to the day cells. Then, we serially constructed novel spike trains by choosing the next interval in the series based on the current interval and iterating up to the required number of spikes for 1 hr of stimulation. Intervals were chosen by rejection sampling of the continuous conditional probability densities of the GMM after discarding 200 burn-in samples. The resulting log intervals were exponentiated and normalized into spike times that were binned into 10 ms binary signals for stimulation. As was the case for the "playback" temporal codes, no bursts were noted in these synthetic temporal codes.

To identify a shorter time window that maintained a similar MFR, we compared local MFRs and global MFRs for all 100 synthetic spike trains by calculating a moving average for sliding window lengths ranging from 100 ms to the entirety of the spike train (1 hr) using 100 ms steps. The CV of the moving averages was then calculated for each sliding window length and plotted versus window length (Figure S6E). Based on both visual inspection and a criterion of CV 0.05, a time window of 40 sec was selected as a shorter time window that maintained a similar MFR compared to the entire 1 hr spike train.

Clock neuron models

We studied parametric variations of a previously published Hodgkin-Huxley-type dynamical model of *Drosophila* circadian neuron excitability (Flourakis et al., 2015) that was based on a prior mammalian suprachiasmatic nucleus model. The model was simulated (0.1 ms timesteps; Runge-Kutta fourth-order method for neurons; EulerMaruyama method for noise) using the equation-based Brian simulator (Goodman and Brette, 2008) and analyzed with custom Python software. The randomized background input shared by the neuron models was simulated as an Ornstein-Uhlenbeck process with 3 pA bandwidth Gaussian noise; we did not inject voltage noise. The equations and parameters of the Flourakis *et al* model (Flourakis et al., 2015) were implemented as described with several variations. The K_{Ca}

conductances were modeled as BK channels. To fix our simulations to the equivalent of mid-day/night (analogous to ZT6–8/ZT18–20 data; cf. Figure 7J of Flourakis *et al*, 2015 (Flourakis et al., 2015)), we set gNALCN = 0.17 nS and gK_{leak} = 0.05 nS. To implement the day/night shift due to Na^+/K^+ modulation, the day/BK neuron models set E_{Na} = 40 mV and E_K = –85 mV and the ATPase/ATPase+BK models set E_{Na} = 51 mV and E_K = –121 mV. The reversal potentials were tuned by finding the Na^+/K^+ concentration change (±1.5 mM) that matched the model RMP to the observed range (day to night: –48 to –64 mV). Further, the day neuron set gNa = 150 nS (instead of 229 nS) to reduce hyperexcitability due to the Na^+/K^+ modulation; the BK/ATPase+BK neurons set gBK = 20 nS (instead of 10 nS); and the ATPase/ATPase+BK neurons set I_{app} = 13 pA (instead of 0 pA), which was the minimal applied current that brought the membrane excitability into the limit cycle regime necessary for spiking.

QUANTIFICATION AND STATISTICAL ANALYSIS

Spike train statistics

To quantify temporal coding, we mainly utilized the coefficient of variation (CV) (Holt et al., 1996) of ISIs, a classical measure of spike time irregularity, which is a global measure defined as the dispersion of the ISIs, (CV_{ISI} = ISI SD/ISI mean). In addition to CV_{ISI}, we also calculated the local coefficient of variation (CV_2) (Holt et al., 1996) and the local variation (LV) (Shinomoto et al., 2003) as alternative measures of local irregularity, by computing the dispersion of the two adjacent ISIs.

CV_2 is defined as =

$$CV_2 = \frac{2\left|ISI_{i+1} - ISI_i\right|}{ISI_{i+1} + ISI_i}$$

LV is defined as

$$Lv = \frac{1}{n-1}\sum_{i=1}^{n-1}\frac{3\left(ISI_i - ISI_{i+1}\right)^2}{\left(ISI_i + ISI_{i+1}\right)^2}$$

where ISI_i is the *ith* ISI and n is the number of ISIs for both. To define the shape of the interspike interval (ISI) histogram, we calculated skewness (which assesses asymmetry) and kurtosis (which assesses "tailedness"). See Kumbhare and Baron, 2015 for further discussion of these variables. For identification of bursting events, we used the following criteria: burst onset, ISI < 80 ms; burst offset, ISI > 160 ms (Grace and Bunney, 1984; Liu et al., 2016).

To address whether STDP may underlie the observed DN1p-PI synaptic plasticity, we analyzed the relative spike timing of presynaptic DN1p and the postsynaptic Dilp2+ PI neurons. To do this, we used our intracellular recordings of Dilp2+ PI neuron spikes and our

optogenetic stimulus pattern as a surrogate for DN1p spikes and quantified their relative timing for all combinations within ± 500 ms.

General statistical analysis

Statistical analyses were performed using Prism software (GraphPad). For comparisons of 2 groups of normally or non-normally distributed data, t-tests or Mann-Whitney Utests were performed, respectively. For multiple comparisons, ANOVAs followed by post-hoc Tukey or multiple t-tests with Holm-Bonferroni correction were performed. For multiple comparisons of non-normally distributed data, Kruskal-Wallis tests were performed, with Bonferroni correction for post-hoc comparisons. Reliability of spike onset rapidness (dVm/dt measured from spike onset threshold to peak dVm/dt) was calculated using Cronbach's alpha. For within cells comparisons, paired t-tests were used.

Supplementary Material

Refer to Web version on PubMed Central for supplementary material.

Acknowledgements

REFERENCES

Adrian ED, and Zotterman Y (1926a). The impulses produced by sensory nerveendings: Part II. The response of a Single End-Organ. The Journal of physiology 61, 151–171. [PubMed: 16993780]

Adrian ED, and Zotterman Y (1926b). The impulses produced by sensory nerve endings: Part 3. Impulses set up by Touch and Pressure. The Journal of physiology 61, 465–483. [PubMed: 16993807]

Bailey CH, Giustetto M, Huang YY, Hawkins RD, and Kandel ER (2000). Is heterosynaptic modulation essential for stabilizing Hebbian plasticity and memory? Nature reviews Neuroscience 1, 11–20. [PubMed: 11252764]

Baranauskas G (2015). Can Optogenetic Tools Determine the Importance of Temporal Codes to Sensory Information Processing in the Brain? Frontiers in systems neuroscience 9, 174. [PubMed: 26733826]

Barber AF, Erion R, Holmes TC, and Sehgal A (2016). Circadian and feeding cues integrate to drive rhythms of physiology in *Drosophila* insulin-producing cells. Genes & development 30, 2596–2606. [PubMed: 27979876]

Blumhagen F, Zhu P, Shum J, Scharer YP, Yaksi E, Deisseroth K, and Friedrich RW (2011). Neuronal filtering of multiplexed odour representations. Nature 479, 493498.

Buzsaki G (2010). Neural syntax: cell assemblies, synapsembles, and readers. Neuron 68, 362–385. [PubMed: 21040841]

Cao G, and Nitabach MN (2008). Circadian control of membrane excitability in *Drosophila melanogaster* lateral ventral clock neurons. The Journal of neuroscience : the official journal of the Society for Neuroscience 28, 6493–6501. [PubMed: 18562620]

Chong E, and Rinberg D (2018). Behavioral readout of spatio-temporal codes in olfaction. Current opinion in neurobiology 52, 18–24. [PubMed: 29694923]

Flourakis M, Kula-Eversole E, Hutchison AL, Han TH, Aranda K, Moose DL, White KP, Dinner AR, Lear BC, Ren D, et al. (2015). A Conserved Bicycle Model for Circadian Clock Control of Membrane Excitability. Cell 162, 836–848. [PubMed: 26276633]

Ghosh A, and Greenberg ME (1995). Calcium signaling in neurons: molecular mechanisms and cellular consequences. Science 268, 239–247. [PubMed: 7716515]

Goldberg JM, Smith CE, and Fernandez C (1984). Relation between discharge regularity and responses to externally applied galvanic currents in vestibular nerve afferents of the squirrel monkey. Journal of neurophysiology 51, 1236–1256. [PubMed: 6737029]

Gollisch T, and Meister M (2008). Rapid neural coding in the retina with relative spike latencies. Science 319, 1108–1111. [PubMed: 18292344]

Goodman D, and Brette R (2008). Brian: a simulator for spiking neural networks in python. Frontiers in neuroinformatics 2, 5. [PubMed: 19115011]

Grace AA, and Bunney BS (1984). The control of firing pattern in nigral dopamine neurons: burst firing. The Journal of neuroscience : the official journal of the Society for Neuroscience 4, 2877–2890. [PubMed: 6150071]

Gray CM, Konig P, Engel AK, and Singer W (1989). Oscillatory responses in cat visual cortex exhibit inter-columnar synchronization which reflects global stimulus properties. Nature 338, 334–337. [PubMed: 2922061]

Guo F, Yu J, Jung HJ, Abruzzi KC, Luo W, Griffith LC, and Rosbash M (2016). Circadian neuron feedback controls the *Drosophila* sleep--activity profile. Nature 536, 292–297. [PubMed: 27479324]

Haddad R, Lanjuin A, Madisen L, Zeng H, Murthy VN, and Uchida N (2013). Olfactory cortical neurons read out a relative time code in the olfactory bulb. Nature neuroscience 16, 949–957. [PubMed: 23685720]

Harris JJ, Jolivet R, and Attwell D (2012). Synaptic energy use and supply. Neuron 75, 762–777. [PubMed: 22958818]

Histed MH, and Maunsell JH (2014). Cortical neural populations can guide behavior by integrating inputs linearly, independent of synchrony. Proceedings of the National Academy of Sciences of the United States of America 111, E178–187. [PubMed: 24367105]

Holt GR, Softky WR, Koch C, and Douglas RJ (1996). Comparison of discharge variability in vitro and in vivo in cat visual cortex neurons. Journal of neurophysiology 75, 1806–1814. [PubMed: 8734581]

Horisberger JD, Jaunin P, Good PJ, Rossier BC, and Geering K (1991). Coexpression of alpha 1 with putative beta 3 subunits results in functional Na+/K+ pumps in *Xenopus* oocytes. Proceedings of the National Academy of Sciences of the United States of America 88, 8397–8400. [PubMed: 1717977]

Huber R, Hill SL, Holladay C, Biesiadecki M, Tononi G, and Cirelli C (2004). Sleep homeostasis in *Drosophila melanogaster*. Sleep 27, 628–639. [PubMed: 15282997]

Ilin V, Malyshev A, Wolf F, and Volgushev M (2013). Fast computations in cortical ensembles require rapid initiation of action potentials. The Journal of neuroscience : the official journal of the Society for Neuroscience 33, 2281–2292. [PubMed: 23392659]

Jaisser F, Jaunin P, Geering K, Rossier BC, and Horisberger JD (1994). Modulation of the Na,K-pump function by beta subunit isoforms. The Journal of general physiology 103, 605–623. [PubMed: 8057080]

Jaramillo AM, Zeng H, Fei H, Zhou Y, and Levitan IB (2006). Expression and function of variants of slob, slowpoke channel binding protein, in *Drosophila*. Journal of neurophysiology 95, 1957–1965. [PubMed: 16339006]

Klapoetke NC, Murata Y, Kim SS, Pulver SR, Birdsey-Benson A, Cho YK, Morimoto TK, Chuong AS, Carpenter EJ, Tian Z, et al. (2014). Independent optical excitation of distinct neural populations. Nature methods 11, 338–346. [PubMed: 24509633]

Kumar A and Mehta MR (2011). Frequency-dependent changes in NMDARdependent synaptic plasticity. Frontiers in computational neuroscience 5, 38. [PubMed: 21994493]

Kumbhare D and Baron MS (2015). A novel tri-component scheme for classifying neuronal discharge patterns. Journal of neuroscience methods 239, 148–161. [PubMed: 25256642]

Kunst M, Hughes ME, Raccuglia D, Felix M, Li M, Barnett G, Duah J, and Nitabach MN (2014). Calcitonin gene-related peptide neurons mediate sleep-specific circadian output in *Drosophila*. Current biology : CB 24, 2652–2664. [PubMed: 25455031]

Lancaster B, and Nicoll RA (1987). Properties of two calcium-activated hyperpolarizations in rat hippocampal neurones. The Journal of physiology 389, 187–203. [PubMed: 2445972]

Laurent G, and Davidowitz H (1994). Encoding of olfactory information with oscillating neural assemblies. Science 265, 1872–1875. [PubMed: 17797226]

Levy WB, and Baxter RA (1996). Energy efficient neural codes. Neural computation 8, 531–543. [PubMed: 8868566]

Liu C, Weaver DR, Strogatz SH, and Reppert SM (1997). Cellular construction of a circadian clock: period determination in the suprachiasmatic nuclei. Cell 91, 855–860. [PubMed: 9413994]

Liu Q, Tabuchi M, Liu S, Kodama L, Horiuchi W, Daniels J, Chiu L, Baldoni D, and Wu MN (2017). Branch-specific plasticity of a bifunctional dopamine circuit encodes protein hunger. Science 356, 534–539. [PubMed: 28473588]

Liu S, Lamaze A, Liu Q, Tabuchi M, Yang Y, Fowler M, Bharadwaj R, Zhang J, Bedont J, Blackshaw S, et al. (2014). WIDE AWAKE Mediates the Circadian Timing of Sleep Onset. Neuron 82, 151–166. [PubMed: 24631345]

Liu S, Liu Q, Tabuchi M, and Wu MN (2016). Sleep Drive Is Encoded by Neural Plastic Changes in a Dedicated Circuit. Cell 165, 1347–1360. [PubMed: 27212237]

Luan H, Lemon WC, Peabody NC, Pohl JB, Zelensky PK, Wang D, Nitabach MN, Holmes TC, and White BH (2006). Functional dissection of a neuronal network required for cuticle tanning and wing expansion in *Drosophila*. The Journal of neuroscience : the official journal of the Society for Neuroscience 26, 573–584. [PubMed: 16407556]

MacKay DM, and McCulloch WS (1952). The limiting information capacity of a neuronal link. The bulletin of mathematical biophysics 14, 127–135.

Markram H, Lubke J, Frotscher M, and Sakmann B (1997). Regulation of synaptic efficacy by coincidence of postsynaptic APs and EPSPs. Science 275, 213–215. [PubMed: 8985014]

Miesenbock G (2011). Optogenetic control of cells and circuits. Annual review of cell and developmental biology 27, 731–758.

O'Connor DH, Hires SA, Guo ZV, Li N, Yu J, Sun QQ, Huber D, and Svoboda K (2013). Neural coding during active somatosensation revealed using illusory touch. Nature neuroscience 16, 958–965. [PubMed: 23727820]

Panzeri S, Brunel N, Logothetis NK, and Kayser C (2010). Sensory neural codes using multiplexed temporal scales. Trends in neurosciences 33, 111–120. [PubMed: 20045201]

Panzeri S, Harvey CD, Piasini E, Latham PE, and Fellin T (2017). Cracking the Neural Code for Sensory Perception by Combining Statistics, Intervention, and Behavior. Neuron 93, 491–507. [PubMed: 28182905]

Piotrkiewicz M (1999). An influence of afterhyperpolarization on the pattern of motoneuronal rhythmic activity. Journal of physiology, Paris 93, 125–133.

Rieke F, Warland D, Steveninck R, and Bialek W (1997). Spikes: Exploring the Neural Code (MIT Press).

Schopperle WM, Holmqvist MH, Zhou Y, Wang J, Wang Z, Griffith LC, Keselman I, Kusinitz F, Dagan D, and Levitan IB (1998). Slob, a novel protein that interacts with the Slowpoke calcium-dependent potassium channel. Neuron 20, 565–573. [PubMed: 9539129]

Shinomoto S, Shima K, and Tanji J (2003). Differences in spiking patterns among cortical neurons. Neural computation 15, 2823–2842. [PubMed: 14629869]

Skaggs WE, McNaughton BL, Wilson MA, and Barnes CA (1996). Theta phase precession in hippocampal neuronal populations and the compression of temporal sequences. Hippocampus 6, 149–172. [PubMed: 8797016]

Smear M, Shusterman R, O'Connor R, Bozza T, and Rinberg D (2011). Perception of sniff phase in mouse olfaction. Nature 479, 397–400. [PubMed: 21993623]

Stein RB (1967). The information capacity of nerve cells using a frequency code. Biophysical journal 7, 797–826. [PubMed: 19210999]

Stiefel KM, Englitz B, and Sejnowski TJ (2013). Origin of intrinsic irregular firing in cortical interneurons. Proceedings of the National Academy of Sciences of the United States of America 110, 7886–7891. [PubMed: 23610409]

Tabuchi M, Lone SR, Liu S, Liu Q, Zhang J, Spira AP, and Wu MN (2015). Sleep interacts with abeta to modulate intrinsic neuronal excitability. Current biology : CB 25, 702–712. [PubMed: 25754641]

Uchida N, Poo C, and Haddad R (2014). Coding and transformations in the olfactory system. Annual review of neuroscience 37, 363–385.

van Alphen B, Yap MH, Kirszenblat L, Kottler B, and van Swinderen B (2013). A dynamic deep sleep stage in *Drosophila*. The Journal of neuroscience : the official journal of the Society for Neuroscience 33, 6917–6927. [PubMed: 23595750]

Wu CL, Xia S, Fu TF, Wang H, Chen YH, Leong D, Chiang AS, and Tully T (2007). Specific requirement of NMDA receptors for long-term memory consolidation in *Drosophila* ellipsoid body. Nature neuroscience 10, 1578–1586. [PubMed: 17982450]

Zhang L, Chung BY, Lear BC, Kilman VL, Liu Y, Mahesh G, Meissner RA, Hardin PE, and Allada R (2010a). DN1p circadian neurons coordinate acute light and PDF inputs to produce robust daily behavior in *Drosophila*. Current biology : CB 20, 591–599. [PubMed: 20362452]

Zhang Y, Liu Y, Bilodeau-Wentworth D, Hardin PE, and Emery P (2010b). Light and temperature control the contribution of specific DN1 neurons to *Drosophila* circadian behavior. Current biology : CB 20, 600–605. [PubMed: 20362449]

Zhang Y, Bucher D, and Nadim F (2017). Ionic mechanisms underlying history-dependence of conduction delay in an unmyelinated axon. eLife 6.

Highlights

–The temporal pattern of clock neuron firing controls sleep quality in Drosophila

–Cyclical ionic fluxes drive changes in spike waveform to generate temporal codes

–These temporal codes are transformed to rate codes in a downstream arousal circuit

–This transformation is via a temporal pattern-dependent form of synaptic plasticity
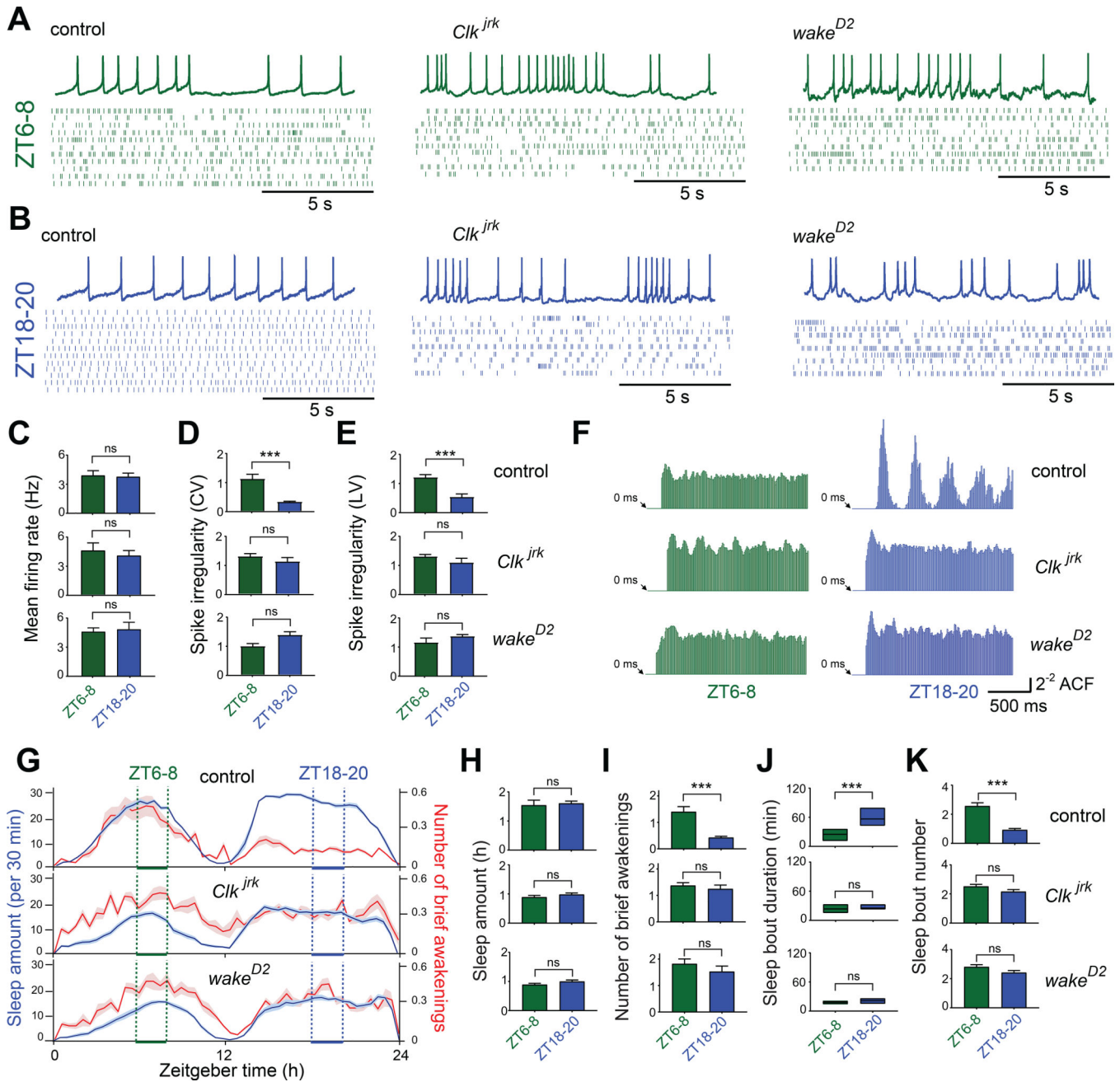
Figure 1. Sleep quality is clock-dependent and associated with distinct temporal spike patterns in DN1p neurons.

(A and B) Representative membrane potential traces and temporal raster plots of spontaneous firing of DN1ps at ZT6–8 (A) and ZT18–20 (B) in control (*left*), *Clk^jrk* (*middle*), and *wake^D2* flies (*right*). Membrane potential traces are shown for a 4 sec window. (C to E) Mean firing rate (C), coefficient of variation (CV) (D), local variation (LV) (E) of spontaneous activity of DN1ps at ZT6–8 and ZT18–20 in *wake-GAL4>UAS-CD8::GFP* in control (*top*, n = 11 for ZT6–8 and n = 12 for ZT18–20), *Clk^jrk* (*middle*, n = 10 and n = 9), or *wake^D2* backgrounds (*bottom*, n = 9 and n = 9). Comparisons were made between (not within) cells.

(F) Autocorrelation function of the spike trains shown in (A) and (B).

(G to K) Sleep amount (blue) and brief awakenings (red) profile (G), sleep amount (H), number of brief awakenings (I), sleep bout duration (J), and sleep bout number (K) for control *wake-GAL4>UAS-CD8::GFP* in control (*top*, n = 67), *Clk^{jrk}* (*middle*, n = 54), and *wake^{D2}* backgrounds (*bottom*, n = 63). In panel G, mid-day (ZT6–8) and mid-night (ZT18–20) time windows are denoted by dashed lines. Error bars here and throughout represent SEM; *p < 0.05, **p < 0.01, ***p < 0.001; ns, not significant. (See also Figures S**Figure S1** and S**Figure S2**, and Table S1).
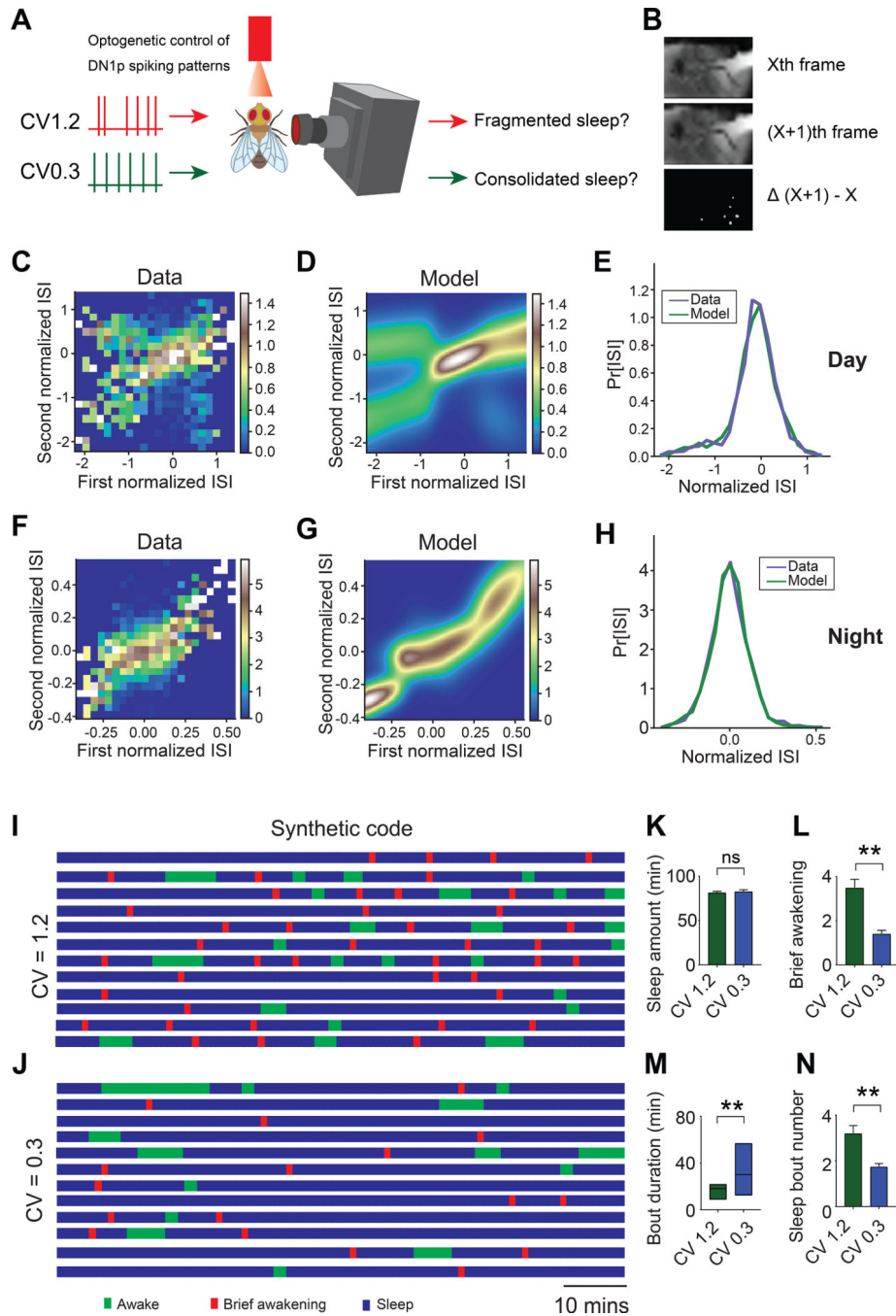
Figure 2. Temporal spike patterns alone are sufficient to determine sleep quality

Schematic illustrating video preparation setup and experimental design.

Example frames from video analysis. Fly movement is defined from the preceding frame (top) and the next consecutive frame (middle) by generating a difference image (bottom) through time (2 frames/s).

(C to H) To generate synthetic codes for stimulation, Gaussian mixture models captured second-order temporal structure for day (ZT6–8, C to E) and night (ZT18–20, F to H) spiking activity. Histograms showing relative frequency of pairs of adjacent spike intervals

in training data; histogram axes are log-scaled; training data were rate-normalized and log-transformed (C and F). Joint densities of the mixture models reveal the temporal structure of the neural code learned from the training data (D and G). Marginal distributions of normalized spike timing from a size-matched random sample of the mixture model (green) closely match the training data (blue), suggesting that the synthetic codes are biologically realistic (E and H).

(I to J) Sleep/wake state plots of individual tethered *R18H11-GAL4>UAS-CsChrimson* flies during optogenetic stimulation of DN1ps using synthetic codes with irregular (I) (CV_{ISI} = 1.2, n=12) and regular (J) (CV_{ISI} = 0.3, n=12) patterns at ZT18–20. Brief awakenings and awake and sleep states are denoted with red, green, and blue bars, respectively.

(K to N) Sleep amount (K), number of brief awakenings (L), sleep bout duration (M), and sleep bout number (N) for the flies shown in I and J. (See also Figures S3 and S4).
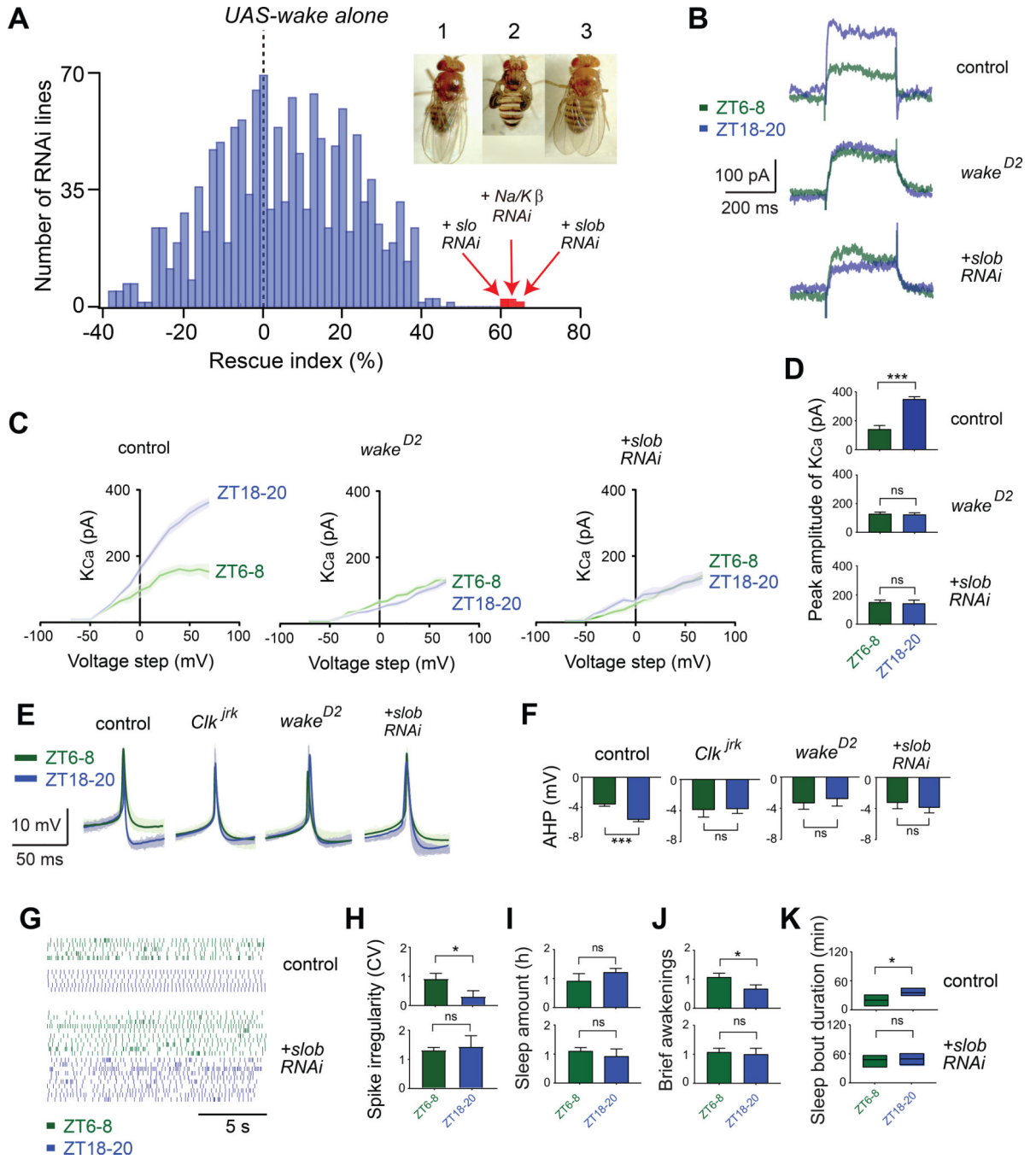
Figure 3. WAKE acts via SLOB to regulate DN1p temporal coding and sleep quality

(A) Histogram showing rescue index of RNAi lines from the *wake* genetic interaction screen (n=1,167 RNAi lines). Inset, 1=*CCAP-GAL4>UAS-CD8::GFP*, 2=*CCAP-GAL4>UAS-wake*, 3=*CCAP-GAL4>UAS-wake, UAS-slob RNAi*.

(B) Representative traces of Ca^{2+}-dependent K^+ current (K_{Ca}) in DN1ps at ZT6–8 (green) and ZT18–20 (blue) in *wake-GAL4>UAS-CD8::GFP*, *wake-GAL4>UAS-CD8::GFP; wake^{D2}*, and *wake-GAL4>UAS-CD8::GFP, UAS-slob RNAi* flies.

(C and D) *I-V* relation of steady-state activation of K_{Ca} current (C) and peak K_{Ca} amplitude at a holding potential of +60 mV (D) from DN1ps at ZT6–8 (green) and ZT1820 (blue) for *wake-GAL4>UAS-CD8::GFP* (n = 8 for ZT6–8 and n = 9 for ZT18–20), *wake-GAL4>UAS-CD8::GFP; wake^{D2}* (n = 7 and n = 7), and *wake-GAL4>UAS-CD8::GFP, UAS-slob RNAi* flies (n = 4 and n = 4).

(E and F) Averaged spike waveforms (E) and peak AHP amplitude (F) of DN1ps at ZT68 (green) and ZT18–20 (blue) in *wake-GAL4>UAS-CD8::GFP* (n = 11 for ZT6–8 and n=12 for ZT18–20), *wake-GAL4>UAS-CD8::GFP; Clk^{jrk}* (n = 10 and 9), *wakeGAL4>UAS-CD8::GFP; wake^{D2}* (n = 9 and 9), and *wake-GAL4>UAS-CD8::GFP, UAS-slob RNAi* flies (n =10 and 9). Note that the AHP data for flies in *Clk^{jrk}* and *wake^{D2}* mutant background are derived from the dataset shown in Fig. 1. Scale bars denote 10 mV and 50 ms.

(G and H) temporal raster plots (G) and CV (H) of spontaneous firing of DN1ps at ZT6–8 (green) and ZT18–20 (blue) in *wake-Gal4>UAS-CD8::GFP* (n=5 for ZT6–8 and n=5 for ZT18–20) and *wake-Gal4>UAS-CD8::GFP, UAS-slob RNAi* flies (n =10 and 9). (I to K) Sleep amount (I), number of brief awakenings (J), and sleep bout duration (K) during ZT6–8 (green) and ZT18–20 (blue) for *R18H11-GAL4>UAS-CD8::GFP* (n = 32) and *R18H11-GAL4>UAS-slob RNAi* flies (n=32). For panels 3D, 3F, and 3H, comparisons were made between (not within) cells. (See also Figures S4 and S5, and Table S1).
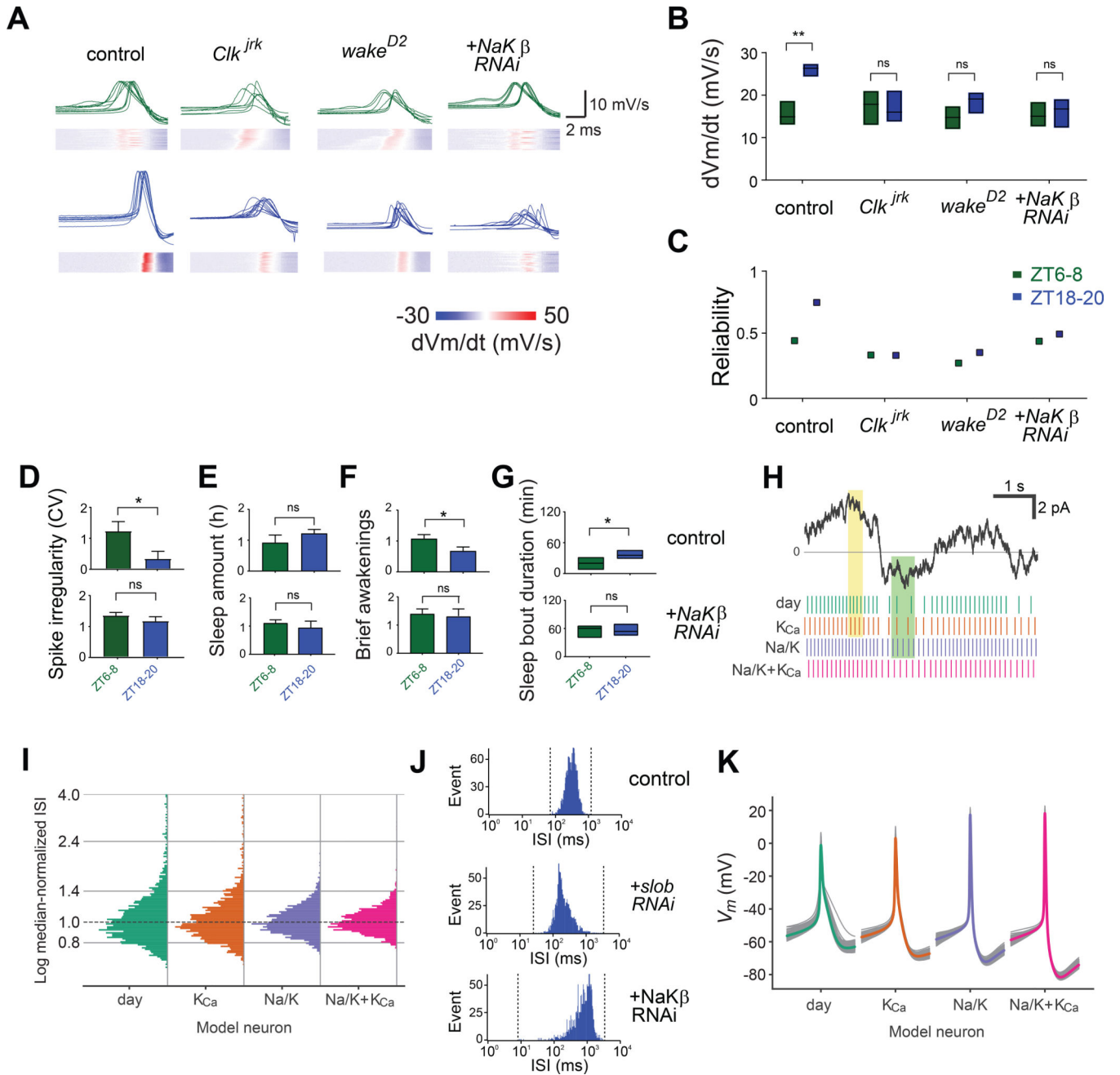
Figure 4. NaKβ is a clock- and WAKE-dependent molecule that modulates DN1p temporal coding and sleep quality

(A to C) Derivatives of the spike wave membrane potential, from spike onset threshold to the peak of the spike, plotted over time (dVm/dt) (A, above) and as heat maps (A, below), the highest dVm/dt from panel A shown as boxplots (B), and reliability of time from spike onset threshold to highest dVm/dt of spikes (C) from DN1ps at ZT6–8 (green) and ZT18–20 (blue) in *wake-GAL4>UAS-CD8::GFP, wake-GAL4>UAS-CD8::GFP; Clk^jrk, wake-GAL4>UAS-CD8::GFP; wake^D2*, and *R18H11-GAL4>UAS-tdTomato, UAS-NaKβ RNAi* flies (n =10 for ZT6–8 and n = 10 for ZT18–20). Data for controls and *Clk^jrk*, and *wake^D2*

mutants are derived from the dataset for Figures 1A and 1B. Each trace in panel A represents the average of at least 165 spontaneous spikes from a single DN1p cell.

(D) CV of spontaneous firing of DN1ps at ZT6–8 (green) and ZT18–20 (blue) in *wakeGAL4>UAS-CD8::GFP* (n =5 For ZT6–8 and n=5 for ZT18–20) and *wake-GAL4>UASCD8:GFP, UAS-NaKβ RNAi* flies (n =9 and 10). For panels B-D, comparisons were made between (not within) cells.

(E to G) Sleep amount (E), number of brief awakenings (F), and sleep bout duration (G) during ZT6–8 (green) and ZT18–20 (blue) for *R18H11-GAL4>UAS-CD8::GFP* (n=33) and *R18H11-GAL4>UAS-NaKβ RNAi* flies (n =54).

(H and I) A Hodgkin-Huxley-type model qualitatively reproduces changes in DN1p temporal variability seen at ZT18–20. Four neuron models were simulated with a shared random input: day (control, representing ZT6–8 activity), increased K_{Ca} conductance, increased Na^+/K^+ ATPase activity, and combined enhancement of Na^+/K^+ ATPase and K_{Ca} function. K_{Ca} modulation was modeled as a two-fold increase in channel conductance, and Na^+/K^+ ATPase modulation was modeled as equilibrated day-night shifts in Na^+ and K^+ reversal potentials. Shared noise (top) generated an irregular spike train in the "day" model; the K_{Ca} model slowed firing during periods of high input (gold highlight), while the Na^+/K^+ ATPase model maintained firing across pauses in the daytime spike train (green highlight), resulting in greater regularity of the spike train in the combined model (H). ISI distributions for simulated spikes were median-normalized (dashed line, median) and log-transformed for comparison (I).

(J) ISI histograms of spontaneous activity for DN1ps at ZT18–20 for *R18H11-GAL4>UAS-tdTomato*, *R18H11-GAL4>UAS-slob-RNAi,* or *UAS-td-Tomato, R18H11GAL4>UAS-NaKβ-RNAi, UAS-td-Tomato*

Note that these data are derived from the same datasets used in Figures 3H and 4D. (K) Average spike shapes for all spikes in a 5 min simulation, with 200 example spike traces shown in gray. (See also Figures S4 and S5, and Table S1).
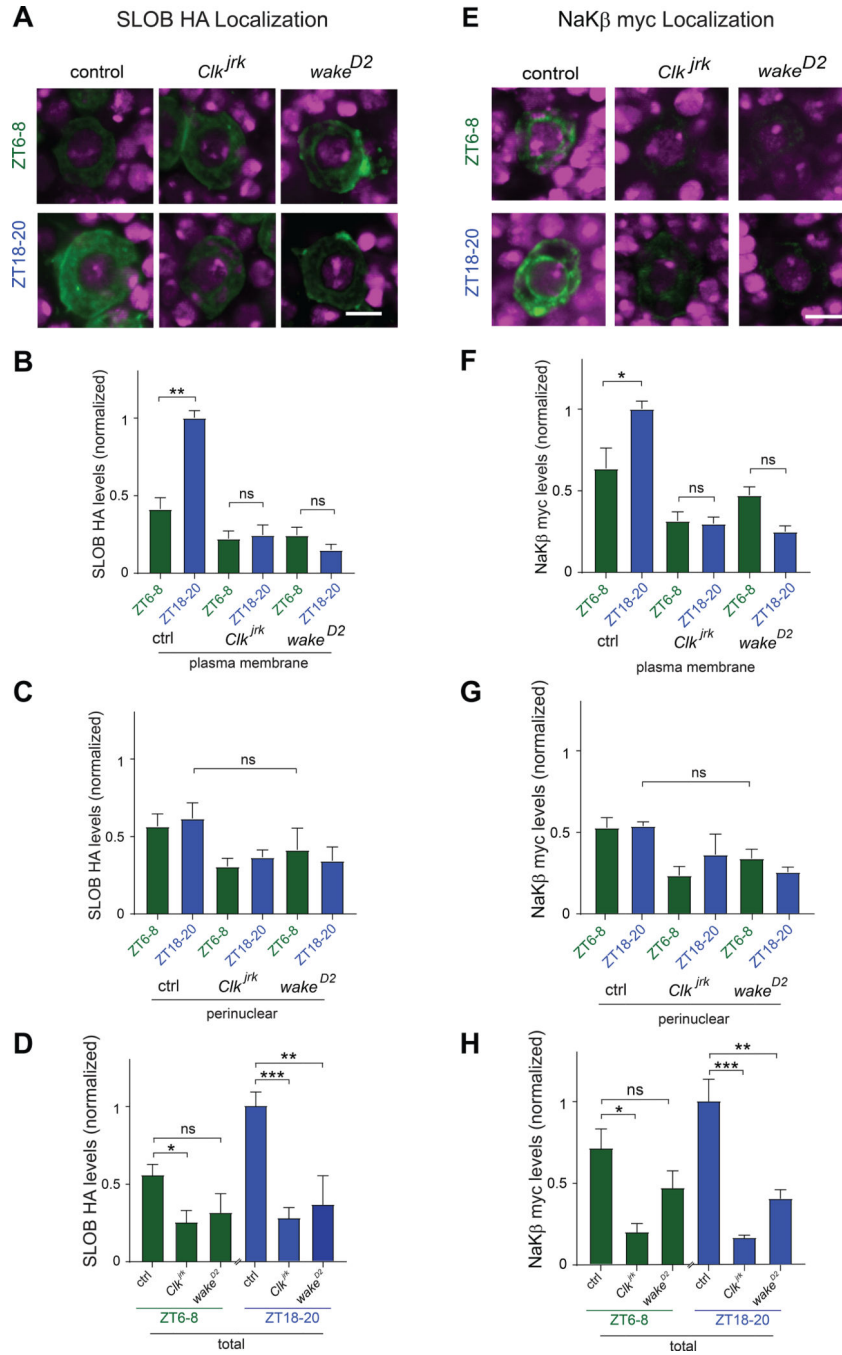
**Figure 5. WAKE regulates membrane targeting of SLOB and NaKβ in a time-dependent manner.**

(A) Immunostaining of l-LNvs with anti-HA (green) with nuclei labeled with DAPI (magenta) in *PDF-GAL4>UAS-slob-HA* flies in control (left), *Clk^jrk^* (middle), and *wake^D2^* (right) backgrounds at ZT6–8 (top) vs. ZT18–20 (bottom). Scale bar indicates 10 μm. (B-D) Quantification of plasma membrane (B), perinuclear (C), and total (D) SLOB-HA levels in l-LNvs at ZT6–8 vs. ZT18–20 in control (n=7 for ZT6–8, and n=10 for ZT18–20), *Clk^jrk^* (n=9 and 9), and *wake^D2^* (n=8 and 8) backgrounds.

(E) Immunostaining of l-LNvs with anti-myc (green) with nuclei labeled with DAPI (magenta) in *PDF-GAL4>UAS-NaKβ–myc* flies in control (left), *Clk^{jrk}* (middle), and *wake^{D2}* (right) backgrounds at ZT6–8 (top) vs. ZT18–20 (bottom). Scale bar indicates 10 μm

(F-H) Quantification of plasma membrane (F), perinuclear (G), and total (H) NaKβ-myc levels in l-LNvs at ZT6–8 vs. ZT18–20 in control (n=11 for ZT6–8, and n=6 for ZT18–20), *Clk^{jrk}* (n=8 and 5), and *wake^{D2}* (n=9 and 9) backgrounds.
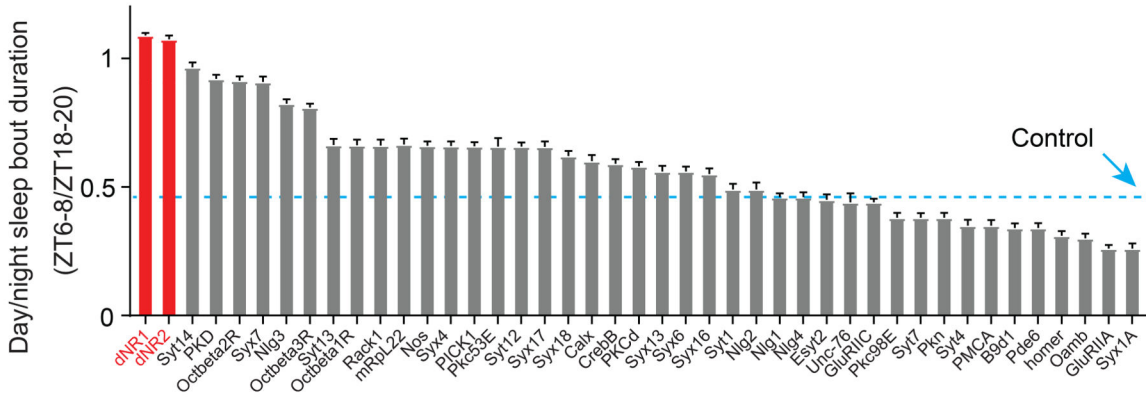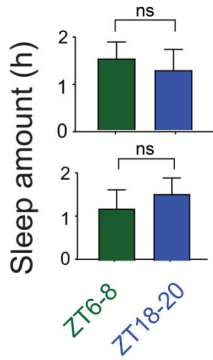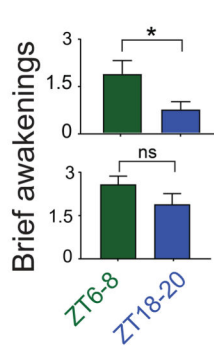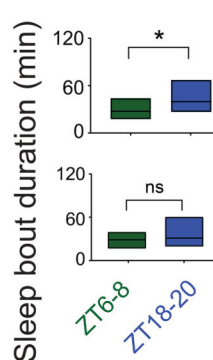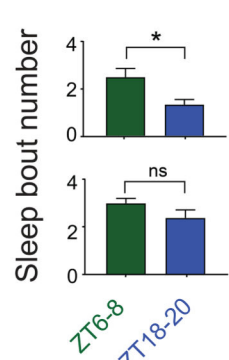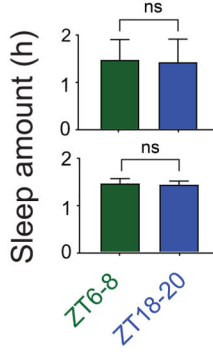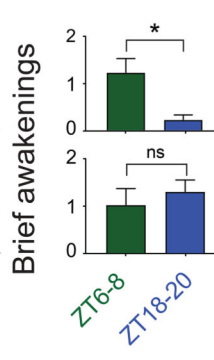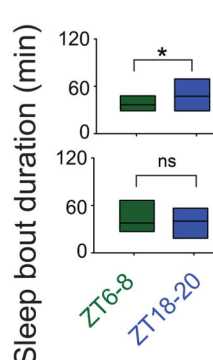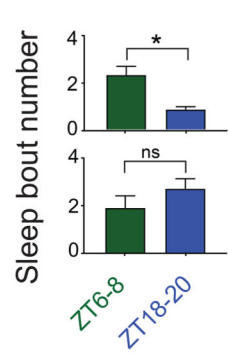
Figure 6. NMDA receptors act in Dilp2+ PI neurons to promote night-time sleep quality

(A) RNAi knockdown screen for Ca^{2+}-related genes that act in Dilp2+ PI neurons to promote sleep quality at night. The day/night sleep bout duration ratio (sleep bout duration for ZT6–8/sleep bout duration for ZT18–20) is plotted, and the blue dashed line indicates the ratio for control *dilp2-GAL4>wt* flies

(B to E) Sleep amount (B), brief awakenings (C), sleep bout duration (D), and sleep bout number (E) during ZT6–8 vs. ZT18–20 for *wt>UAS-dsNR1* control flies (n=32) and *dilp2GAL4>UAS-dsNR1* (n=58).
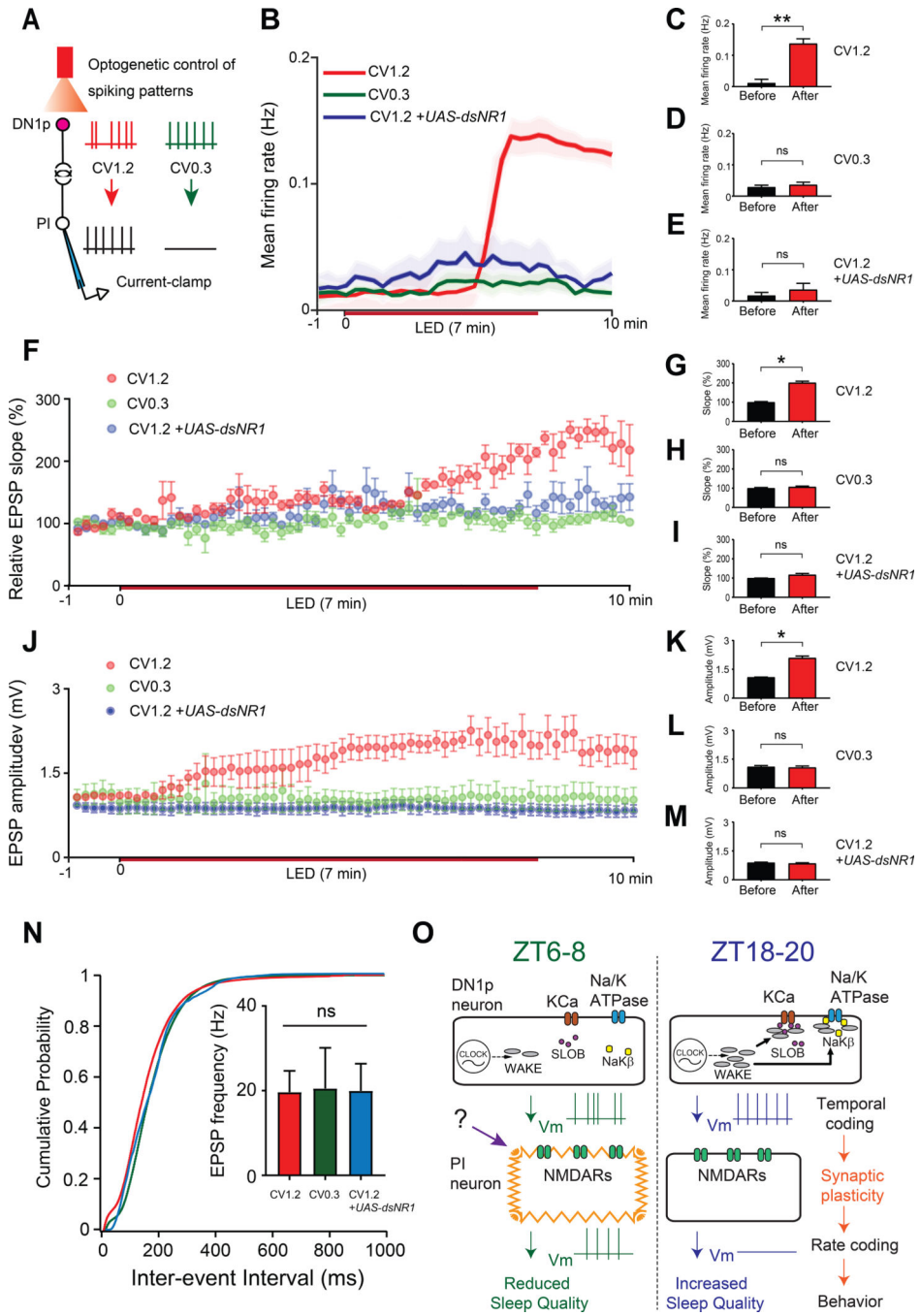
(F to I) Sleep amount (F), brief awakenings (G), sleep bout duration (H), and sleep bout number (I) during ZT6–8 vs. ZT18–20 for *wt>UAS-dsNR2* control flies (n=32) and *dilp2GAL4>UAS-dsNR2* (n=64).

Figure 7. DN1p temporal codes are transformed to downstream rate coding changes, via plasticity-dependent potentiation of DN1p-PI synapses.

(A) Schematic: regular (CV=0.3) or irregular (CV=1.2) firing patterns were optogenetically induced in DN1ps using synthetic temporal codes, while intracellular current-clamp recordings were performed from Dilp2+ PI neurons in a tethered fly. (B) potentiation of Dilp2+ PI neuron firing rate (calculated in 20 sec bins) in response to specific DN1p temporal codes, for *R18H11-LexA, dilp2-Gal4>LexAop-CsChrimson, UAS-GCaMP6s* with CV=0.3 (green, n=3), CV=1.2 (red, n=4), or CV=1.2 in the presence of *UAS-dsNR1* (blue, n=3) at ZT18-ZT20.

(C to E), mean firing rate of Dilp2+ PI neurons for the 1 min bins just prior to ("before) and just after ("after") LED stimulation for synthetic temporal codes CV=1.2 (C), CV=0.3 (D), and CV=1.2 in the presence of *UAS-dsNR1* (E). Comparisons were made within cells

(F) Time course plot of the normalized EPSP rising slope for events in 10 sec bins for CV=1.2 (red circles), CV=0.3 (green circles), and CV=1.2 in the presence of *UAS-dsNR1* (blue circles).

(G to I) Quantification of EPSP rising slope for the 1 min bins just prior to ("before") and just after ("after") LED stimulation for synthetic temporal codes CV=1.2 (G), CV=0.3 (H), and CV=1.2 in the presence of *UAS-dsNR1* (I). Comparisons were made within cells. </p/>(J) Time course plot of EPSP amplitude for events in 10 sec bins for CV=1.2 (red circles), CV=0.3 (green circles), and CV=1.2 in the presence of *UAS-dsNR1* (blue circles).

(K to M) Quantification of EPSP amplitude for the 1 min bins before and after LED stimulation for CV=1.2 (K), CV=0.3 (L), and CV=1.2 in the presence of *UAS-dsNR1* (M). Comparisons were made within cells.

Cumulative frequency plots of EPSP events (N) and quantification of EPSP frequency (inset) for CV=1.2 (red), CV=0.3 (green), or CV=1.2 + *UAS-dsNR1* (blue). Data for F to N are from the same flies as in B-E. Red bar indicates duration of DN1p optogenetic stimulation. Model for how clock-dependent temporal coding drives synaptic plasticity to induce changes in downstream rate coding and enable circadian regulation of sleep behavior. The DN1p clock neurons exhibit irregular firing during the day (ZT6–8). Irregular, but not regular, firing of the DN1ps triggers NMDA receptor-dependent plastic changes in the downstream arousal-promoting Dilp2+ PI neurons, leading to an increase in firing rate of these PI neurons and reduced sleep quality during the day. Note that additional inputs to the PI neurons are also likely required. At night (right), the circadian clock acts via WAKE to upregulate SLOB and NaKβ to increase K_{Ca} current and Na$^+$/K$^+$ ATPase activity to rhythmically alter biophysical properties of spikes to promote regular firing, which leads to reduced firing of the Dilp2+ PI neurons and greater sleep quality. (See also Figure S6).